The Astrophysical Journal, 806:189 (21pp), 2015 June 20 doi:10.1088/0004-637X/806/2/189

LINKING GALAXIES TO DARK MATTER HALOS AT $z \sim 1$: DEPENDENCE OF GALAXY CLUSTERING ON STELLAR MASS AND SPECIFIC STAR FORMATION RATE

Jae-Woo Kim[1], Myungshin Im[1], Seong-Kook Lee[1], Alastair C. Edge[2], David A. Wake[3,4], Alexander I. Merson[5], and Yiseul Jeon[1]
[1] Center for the Exploration of the Origin of the Universe, Department of Physics and Astronomy, Seoul National University, Seoul, Korea; kjw0704@astro.snu.ac.kr, mim@astro.snu.ac.kr
[2] Institute for Computational Cosmology, Department of Physics, University of Durham, South Road, Durham, UK
[3] Department of Astronomy, University of Wisconsin, Madison, WI 53706, USA
[4] Department of Physical Sciences, The Open University, Milton Keynes, UK
[5] Department of Physics and Astronomy, University College London, Gower Place, London, UK
Received 2014 August 11; accepted 2015 May 5; published 2015 June 17

ABSTRACT

We study the dependence of angular two-point correlation functions on stellar mass (M_*) and specific star formation rate (sSFR) of $M_* > 10^{10} M_\odot$ galaxies at $z \sim 1$. The data from the UK Infrared Telescope Infrared Deep Sky Survey Deep eXtragalactic Survey and Canada–France–Hawaii Telescope Legacy Survey cover 8.2 deg^2 sample scales larger than 100 h^{-1} Mpc at $z \sim 1$, allowing us to investigate the correlation between clustering, M_*, and star formation through halo modeling. Based on halo occupation distributions (HODs) of M_* threshold samples, we derive HODs for M_* binned galaxies, and then calculate the $M_*/M_{\rm halo}$ ratio. The ratio for central galaxies shows a peak at $M_{\rm halo} \sim 10^{12} h^{-1} M_\odot$, and satellites predominantly contribute to the total stellar mass in cluster environments with $M_*/M_{\rm halo}$ values of 0.01–0.02. Using star-forming galaxies split by sSFR, we find that main sequence galaxies ($\log$ sSFR/yr$^{-1} \sim -9$) are mainly central galaxies in $\sim 10^{12.5} h^{-1} M_\odot$ halos with the lowest clustering amplitude, while lower sSFR galaxies consist of a mixture of both central and satellite galaxies where those with the lowest M_* are predominantly satellites influenced by their environment. Considering the lowest $M_{\rm halo}$ samples in each M_* bin, massive central galaxies reside in more massive halos with lower sSFRs than low mass ones, indicating star-forming central galaxies evolve from a low M_*–high sSFR to a high M_*–low sSFR regime. We also find that the most rapidly star-forming galaxies ($\log$ sSFR/yr$^{-1} > -8.5$) are in more massive halos than main sequence ones, possibly implying galaxy mergers in dense environments are driving the active star formation. These results support the conclusion that the majority of star-forming galaxies follow secular evolution through the sustained but decreasing formation of stars.

Key words: galaxies: evolution – galaxies: halos – large-scale structure of universe

1. INTRODUCTION

It is expected that small structures merge to form more massive ones in the lambda cold dark matter (ΛCDM) paradigm. Therefore small dark matter halos are the seeds for larger structures. Galaxies form in these dark matter halos through the binding of baryons and the cooling of gas (White & Rees 1978). Since galaxies evolve in their host halos, the distribution and evolution of galaxies are tightly related to their host dark matter halos (Baugh 2006). In the context of hierarchical structure formation models, massive dark matter halos can contain many galaxies with a wide range in mass. Furthermore, the population of member galaxies depends on the properties of their host dark matter halo, because the potential well of the dark matter halo affects the properties of galaxies within it.

A popular method for measuring the distribution of galaxies is the two-point correlation function, which describes the excess probability of a galaxy pair over a random distribution on specific scales (Peebles 1980). Recently, wide and deep surveys have provided opportunities to study the dependence of the clustering of galaxies on their various intrinsic properties such as color, luminosity, stellar mass and population (Norberg et al. 2001, 2002; Zehavi et al. 2002, 2005; Coil et al. 2008; Ross & Brunner 2009a; Loh et al. 2010; Ross et al. 2010; Zehavi et al. 2011). As a result, it is known that redder, brighter or more massive galaxies are more strongly clustered than those having opposite properties.

For high redshift galaxies, one of the most efficient selection methods is to use their observed color. Thus, many previous studies have applied various color cuts to select high redshift galaxies such as Extremely Red Objects (Elston et al. 1988; Daddi et al. 2000; Im et al. 2002; Roche et al. 2002, 2003; Yan et al. 2004; Brown et al. 2005; Kong et al. 2006; Gonzalez-Perez et al. 2009; Kong et al. 2009; Kim et al. 2011; Palamara et al. 2013; Kim et al. 2014), BzK galaxies (Daddi et al. 2004; Kong et al. 2006; Hartley et al. 2008; McCracken et al. 2010; Hanami et al. 2012; Merson et al. 2013) and Distant Red Galaxies (Franx et al. 2003; Grazian et al. 2006; Foucaud et al. 2007; Quadri et al. 2008; Guo & White 2009). Their clustering properties also show similar trends to those of low redshift galaxies. Although color selection is efficient in isolating galaxies in a specific redshift range, a simple color cut often extracts a mix of galaxies with different properties and redshift. Hence to correctly trace galaxy clustering it is necessary to measure it from a sample containing galaxies with well defined intrinsic properties and a narrower range in redshift.

The halo occupation distribution (HOD) framework makes it possible to interpret the galaxy clustering in relation to their host dark matter halos (Jing et al. 1998; Benson et al. 2000; Ma & Fry 2000; Peacock & Smith 2000; Seljak 2000; Scoccimarro

et al. 2001; Berlind & Weinberg 2002; Cooray & Sheth 2002). The HOD quantifies the mean number of central or satellite galaxies in a given halo mass (Kravtsov et al. 2004; Zheng et al. 2005). Based on the halo model analysis with multiwavelength data sets, many authors have reported that massive or luminous galaxies are found in more massive halos (Zheng et al. 2007; Ross & Brunner 2009a; Wake et al. 2011; Zehavi et al. 2011; Coupon et al. 2012).

However, the HOD framework fits the number density of galaxies and their clustering simultaneously so we require a large number of galaxies to sufficiently constrain the parameters of both. Also, to avoid the effects of cosmic variance, these galaxies need to be mapped over a large area of sky. The lack of large, sensitive near-IR detectors has prevented identification of a large number of galaxies at $z \geqslant 1$, where the bulk of stellar emission is observed in a near-IR regime. So far, previous work on stellar mass limited galaxies at high redshifts has been based on survey data with areas from a few hundreds arcmin^2 to <1.7 deg^2 (Meneux et al. 2008, 2009; Foucaud et al. 2010; Hartley et al. 2010; Furusawa et al. 2011; Wake et al. 2011; Hartley et al. 2013). Furthermore, this small surveyed area makes it difficult to measure reliable clustering strengths on larger scales (a few tens h^{-1} Mpc), where the distribution of dark matter halos is imprinted, since these surveys have covered at most ~50 h^{-1}Mpc at $z \sim 1$ on a side. Therefore it is important to perform this analysis with homogeneous galaxy samples drawn from a wide-area near-IR survey.

In terms of galaxy evolution, different mechanisms play key roles at different epochs. Peng et al. (2010) proposed that mass quenching is important for all galaxies, but environment quenching dominates at low redshift and at lower masses. Also, there have been many results about the stellar mass function of passive galaxies from wide field optical–near-IR data sets, showing relatively mild evolution of the most massive galaxies but a dramatic change for low mass ones (Drory et al. 2009; Ilbert et al. 2010; Bezanson et al. 2012; Ilbert et al. 2013; Moustakas et al. 2013; Muzzin et al. 2013; Tinker et al. 2013; Tomcjak et al. 2014), which is consistent with the model in Peng et al. (2010). In addition, the evolution of the luminosity function of Luminous Red Galaxies (LRGs) follows a passive evolution model at $z < 0.6$ (Wake et al. 2006). Scoville et al. (2013) reported that the fraction of early type galaxies increases from 30% at $z \sim 1.1$ to 80% at $z \sim 0.2$ in the densest regions, but from 30% to only 50% in low density regions. These results suggest that the dependence of galaxy properties on their host halos at $z \sim 1$ is different from that in the local universe.

Furthermore, the relation between galaxy properties and their environment at $z \sim 1$ is still controversial. Elbaz et al. (2007) and Cooper et al. (2008) found a reversed relation between star formation rate (SFR) and environment at $z \sim 1$, meaning a higher SFR was observed in the highest density regions. Scoville et al. (2013) found the evolution of the relation as a function of redshift, and recover a weak or no dependence of SFR on environment at $z \sim 1$. On the other hand, Cooper et al. (2010), Chuter et al. (2011) and Quadri et al. (2012) reported that the color (or SFR)–density relation persists out to $z \sim 1.5$. Tinker et al. (2013) argued that the central galaxies in low mass halos are likely to be star-forming galaxies at $z \sim 1$, and their evolution contributes to the observed change in the red sequence. However, there are not many results connecting galaxy properties with their host halos at $z \sim 1$, especially detailed, statistical studies based on a large sample from wide area surveys ($\gtrsim$2–3deg^2). Mostek et al. (2013) measured the clustering strength of galaxies with various criteria such as stellar mass, SFR and specific star formation rate (sSFR) at $z \sim 1$ from a small area spectroscopic survey. We re-address their work with a much larger photometric data set making it possible to split galaxies into finer sub-samples.

In this work, we use wide and deep multiwavelength data sets with *ugrizJ*- and *K*-bands based on the UK Infrared Telescope (UKIRT) Infrared Deep Sky Survey (UKIDSS) Deep eXtragalactic Survey (DXS) and Canada–France–Hawaii Telescope (CFHT) Legacy Survey (CFHTLS)–Wide. The catalog covers 8.2 deg^2 with the limit magnitude of $J_{AB} = 23.2$. This is one of the best data sets to investigate the clustering properties of homogeneous galaxy sub-samples and to minimize the influence of cosmic variance, thanks to its unique combination of depth and area. Furthermore, these data allow us to link galaxies with various criteria to their host halos separately. Using this catalog, we measure the angular two-point correlation function of $z \sim 1$ galaxies split into several sub-samples based on stellar mass and sSFR. Additionally, we fit a halo model and measure the bias factor with the measured correlation function in order to link galaxies with their host dark matter halos.

In Section 2, we briefly describe each survey and how the catalog was generated. In Section 3 we note the methods applied to select samples, to measure clustering and to model the HOD. The dependence of galaxy clustering on stellar mass and the stellar mass to halo mass relation are described in Section 4. We present the dependence on sSFRs in Section 5. We also relate these results to the evolution of galaxies in Section 6, and finally summarize this work in Section 7. Throughout this paper, M_* indicates a stellar mass of galaxies and $M_{\rm halo}$ means a dark matter halo mass. We assume a flat ΛCDM cosmology: $\Omega_m = 0.27$, $\sigma_8 = 0.8$, $H_0 = 100\,h$ km s^{-1} Mpc^{-1} with $h = 0.71$. The photometry is quoted in the AB system.

2. DATA

2.1. UKIDSS DXS

The DXS (A. C. Edge et al. 2015, in preparation) is a sub-survey of the UKIDSS which was performed from 2005 to 2012 (Lawrence et al. 2007) using the UKIRT. The DXS images were obtained using the Wide Field Camera (WFCAM, Casali et al. 2007) composed of four Rockwell Hawaii-II 2 K × 2 K array detectors covering four 13.7 × 13.7 arcmin^2 regions. Since WFCAM has a relatively large pixel scale as 0.″4/pixel, a microstepping technique has been applied so that a science image has 0.″2/pixel and avoids an undersampled point-spread function.

The DXS maps ~35 deg^2 composed of 4 different 8.75 deg^2 patches (XMM-LSS, Elain-N1, Lockman Hole and SA22) with aimed depths of $J_{AB} = 23.2$ and $K_{AB} = 22.7$ at a 5σ point-source sensitivity. The actual data show a 90% point-source completeness at these magnitudes (Kim et al. 2011). The scientific goals of the survey are to determine the abundance of galaxy clusters at $z > 1$, to understand the clustering of galaxies, and to investigate the census of the luminosity density in star formation.

In this study, we deal with the SA22 field centered on $\alpha = 22^h17^m00^s$ and $\delta = +00°20'00''$ (J2000). In the whole surveyed area ($3.4 \times 2.6\,\mathrm{deg}^2$), we perform our analysis with images from the UKIDSS data release 9 (DR9) covering ~8 deg^2, and one remaining WFCAM field (~0.7 deg^2) which was not released in DR9 comes from DR10. The area coverage corresponds to roughly 140 h^{-1}Mpc × 107 h^{-1}Mpc at $z = 1$. The average seeing is ~0.″8 in both J and K. The photometric and astrometric solutions are based on the output from the standard pipeline, and are accurate to better than 2% and ~0.″05 (Dye et al. 2006; Lawrence et al. 2007).

2.2. CFHTLS

The CFHTLS[6] is a set of deep and wide optical surveys performed using the MegaCam camera mounted on the CFHT with *ugriz* filters. Of the three surveys that constitute the CFHTLS, we deal with the CFHTLS–Wide W4 field which covers the DXS SA22 area. The CFHTLS W4 field covers 25 deg^2 with limiting magnitudes (50% completeness for point sources) of $u \sim 26.0$, $g \sim 26.5$, $r \sim 25.9$, $i \sim 25.7$ and $z \sim 24.6$ (Gwyn 2012). For this work, we use CFHTLS images taken from the MegaPipe data pipeline at the Canadian Astronomy Data Centre (Gwyn 2012). The image reduction procedure, as well as photometric and astrometric calibrations are well described in Gwyn (2012).

The UKIDSS DXS area is located in the southeast corner of the CFHTLS W4 field. Thus we extract only the sub-region that overlaps with the UKIDSS DXS field. We use the images in all the CFHT filters, i.e., u, g, r, i, and z.

2.3. Catalog

Our main goals in this work are to measure the clustering of galaxies at $z \sim 1$ and to investigate how the clustering of galaxies correlates with the star formation activity and stellar mass of these galaxies. Therefore it is important to accurately determine colors of galaxies to perform spectral energy distribution (SED) fits to estimate galaxy properties as well as to determine their photometric redshifts. In an attempt to improve the photometric accuracy, we generate a new catalog instead of using the released catalogs from the UKIDSS team via WFCAM Science Archive.[7] The new catalog of objects was constructed using the procedure below.

First, since fluxes must be measured from the same region of galaxies at different bands to obtain accurate color, images are convolved through a Gaussian filtering to unify the FWHM. The worst seeing condition of our UKIRT data set is used as a reference, which corresponds to a FWHM of 1.″1. Then we resample all images to have the WFCAM field of view with a four pointing observation and CFHT pixel scale, using the Swarp software (Bertin et al. 2002). Hence, we have 12 images for each band, each covering 0.8 deg^2. We refer to each 0.8 deg^2 image as a tile. The coordinate offsets (ΔR.A. and Δdecl.) between both surveys are 0.″05 and 0.″04, respectively, which are accurate enough to align images.

Second, we run the SExtractor software (Bertin & Arnouts 1996) in dual mode on each tile of the covered area. The unconvolved J-band image is used for the detection and the measurement of AUTO magnitudes which we consider a proxy of total magnitudes of an object. In order to measure the color of each object, 2″ diameter apertures are used to derive aperture magnitudes on the Gaussian filtered images in all bands.

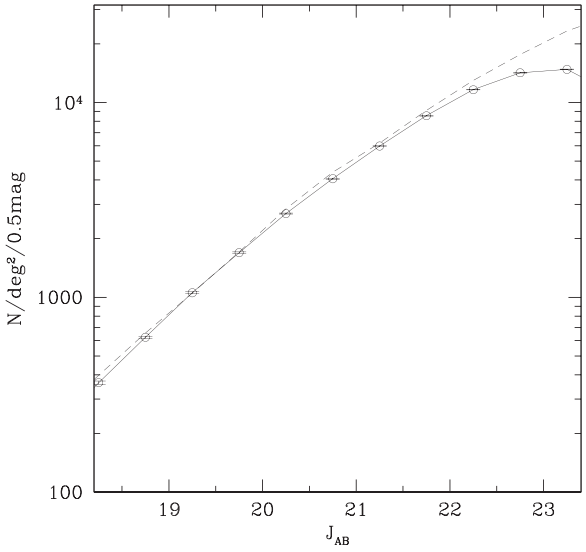

Figure 1. Number counts of galaxies in the DXS SA22 field. The solid line is for all galaxies in this work. Dashed line is the result from Jarvis et al. (2013). Our result is consistent with previous results up to $J_{AB} \sim 22.5$.

Third, spurious objects such as cross-talk and objects on diffraction spikes are removed. It is well known that bright stars make cross-talk at specific positions on the WFCAM chip (Dye et al. 2006). In addition, the unreliable regions of halos or diffraction spikes of bright stars are also masked. We follow the algorithm in Kim et al. (2011) for reducing spurious objects. The masking region for CFHTLS is taken from the Megapipe data pipeline.

Finally, all sub-catalogs from different tiles are merged to create a single, master catalog. If objects have been detected in an overlapping region of different tiles, a 1″ matching radius was applied to identify objects in common for both tiles and the weighted-mean of fluxes from different tiles are assigned as the final flux of uniquely identified objects. Additionally, the Galactic extinction is corrected based on the dust map from Schlegel et al. (1998). In total, ~0.86 million objects are found in the 8.2 deg^2 UKIDSS DXS area. Figure 1 shows the number counts of all galaxies in the DXS area (solid line). Stars were excluded using $(g - z)$ and $(z - K)$ colors, which is similar to the BzK diagram (Daddi et al. 2004; Oi et al. 2014). Figure 2 displays all detected objects in a single tile (0.8 deg^2) with $J < 22.5$ as an illustration. The line indicates the criterion, $(z - K) = 0.44(g - z) - 0.52$, which we apply to distinguish galaxies from stars. The number counts from Jarvis et al. (2013) are also indicated with a dashed line in Figure 1. Our result shows a relatively good agreement over the whole magnitude range. However, we may miss some galaxies in the faint regime ($J_{AB} > 22.5$) due to the relatively shallow depth of CFHTLS and the associated incompleteness. In fact, the distribution of objects shows a large scatter in their colors in the faintest magnitudes, where the magnitude of optical bands is close to the limiting magnitude, making it difficult to distinguish galaxies from the stellar locus. In addition, the 90% completeness for extended sources is ~0.3–0.5 mag brighter than that for point sources. We note that we will apply

[6] http://www.cfht.hawaii.edu/Science/CFHTLS/
[7] http://surveys.roe.ac.uk/wsa/

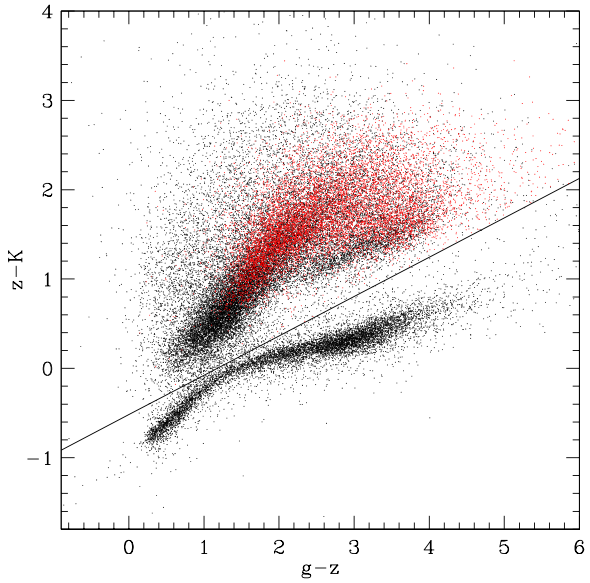

Figure 2. $(z - K)$ vs. $(g - z)$ two-color diagram. We extract objects in a single tile (0.8 deg^2) with $J < 22.5$ for a display purpose (black dots). The line indicates the criterion to distinguish galaxies from stars. Stars fall below the solid line. Red dots are objects satisfying our selection criteria for the analysis in Section 3.1. For display purposes, ~10,000 objects are shown.

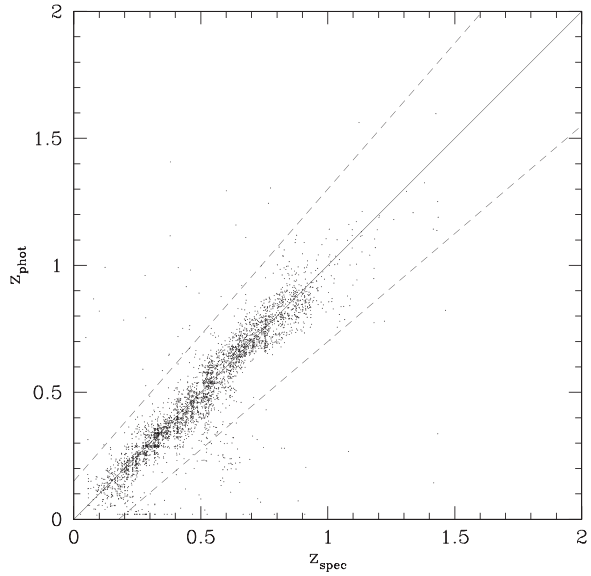

Figure 3. Photometric redshifts ($z_{\rm phot}$) vs. spectroscopic redshifts ($z_{\rm spec}$) for objects observed by the VVDS survey. The dashed lines indicate $\Delta z/(1 + z) = 0.15$.

additional criteria of galaxy stellar mass ($M_* > 10^{10} M_\odot$) and photometric redshift ($0.8 < z < 1.2$) for our analysis, so that we select relatively bright galaxies which are well separated from the stellar locus so we expect negligible stellar contamination in our sample. Red dots in Figure 2 are the objects satisfying our selection criteria. For display purposes, we display a portion of full samples.

3. METHODS

3.1. Selection

This section describes the basic measurement for galaxy properties and the criteria for our sample selection with the multiwavelength catalog from *u*-band to *K*-band corresponding to the rest-frame UV to near-IR for $z \sim 1$ galaxies.

3.1.1. Photometric Redshift

The redshift information is crucial to estimate galaxy properties and to investigate the clustering of galaxies in a specific redshift range. Using our multiwavelength catalog, we estimate the photometric redshift of each object.

We used the *Le Phare* (Arnouts et al. 1999; Ilbert et al. 2006) software to derive photometric redshifts. We used 66 SED templates applied for the CFHTLS–Deep fields in Ilbert et al. (2006). The templates are based on Ell, Sbc, Scd and Irr spectra from Coleman et al. (1980) and a starburst SED from Kinney et al. (1996), and cover the wavelength range from rest-frame UV to near-IR (see Ilbert et al. 2006 for more details). The *Le Phare* code produces offsets in magnitude in each band after running the code on a training set of galaxies for which spectroscopic redshifts are available. The application of the magnitude offset improves the photometric redshift accuracy, and as a training set, we used the VIMOS-VLT Deep Survey (VVDS) wide which is a spectroscopic survey mapping 4 deg^2 of the UKIDSS DXS SA22 area for $I < 22.5$ objects (Le Févre et al. 2005; Garilli et al. 2008). We select 3609 galaxies in the SA22 field having reliable spectroscopic redshift information as a training set. First, we ran the *Le Phare* software for the cross-matched objects between UKIDSS DXS and VVDS to calculate the magnitude offset for each band compared to those from templates, which are ~0.25 mag for *J*-band and less than 0.08 mag for the others. The large offset in *J*-band appear in other works (e.g., Ilbert et al. 2009), and can be understood as due to a template mismatch. In this case, the redshift was fixed with that from VVDS. After finding and then applying these magnitude offsets to the objects in the catalog, the *Le Phare* software was run again for all detected objects. Figure 3 displays the comparison between measured photometric redshifts ($z_{\rm phot}$) and VVDS spectroscopic redshifts ($z_{\rm spec}$) for the cross-matched galaxies. We find that the normalized median absolute deviation of photometric redshift in $\Delta z/(1 + z)$ is ~0.038. For galaxies with $0.8 < z_{\rm spec} < 1.2$ that are studied in this work, the uncertainty is ~0.042. The fraction of outliers ($|\Delta z/(1 + z)| > 0.15$) is <5% for both cases. The dashed lines in Figure 3 show where $\Delta z/(1 + z) = 0.15$. Hereafter the term redshift (z) indicates the photometric result ($z_{\rm phot}$). We use photometric redshifts only for the analysis. We also note that the magnitude offset is applied for the estimation of photometric redshifts only. The magnitude offset improves the photometric redshift estimation by removing a systematic offset of $\Delta z = 0.04$.

Finally, we apply a redshift cut of $0.8 < z < 1.2$, and remove Galactic stars based on the *gzK* diagram as described in Section 2.3. Note that no magnitude cuts are applied when deriving photometric redshifts. In total 141,947 galaxies in this redshift range are used for estimating stellar masses and star formation activity.

In order to check how efficiently the use of photometric redshifts captures galaxies at $0.8 < z < 1.2$, we use a galaxy mock catalog from the GALFORM semi-analytical model (Cole et al. 2000; Merson et al. 2013). For this test, *J*-band magnitudes are randomly scattered in the photometric uncertainty ranges as a function of magnitude, and we selected galaxies satisfying $J < 23.2$, which is the magnitude limit in

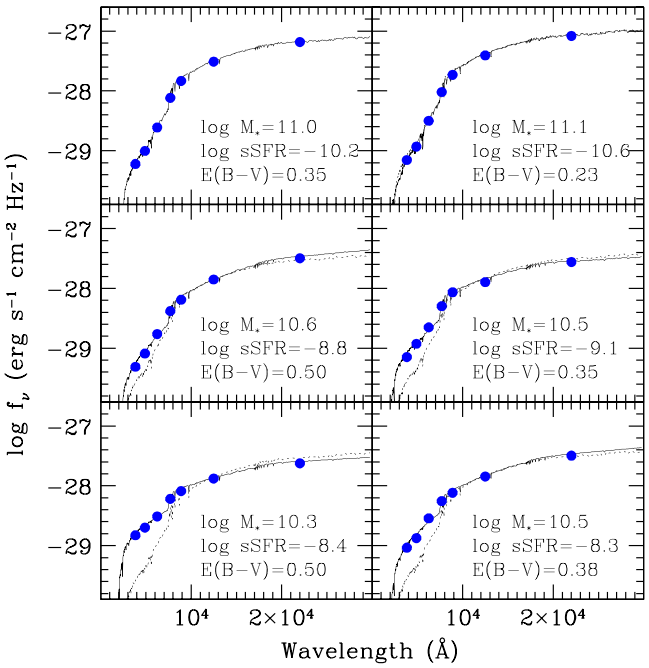

Figure 4. Examples of best fit SEDs (solid line) with observed fluxes (points) for galaxies at $z \sim 1$. Stellar mass and sSFR values of each galaxy are noted in each panel with units in $M_\odot$ and yr^{-1}, respectively. The dotted line is the passive galaxy SED in the top-left panel with normalizing to the flux at 1.2 μm of each object.

the observed catalog. We also randomly assign the redshift uncertainty to the mock galaxies. Then we compare the number of galaxies selected with modified redshifts to that with true redshifts. We find through this test that the use of photometric redshifts can recover 90% of galaxies with true redshifts at $0.8 < z < 1.2$, while the interlopers (foreground or background galaxies) are about 13% among galaxies at $0.8 < z < 1.2$.

3.1.2. SED Fit

In order to estimate stellar masses (M_*) and SFRs of galaxies, we fit model templates of synthetic stellar populations to the multi-band photometry following the algorithm of Lee et al. (2010, 2014). Here we briefly note the assumptions made in this analysis. We use SED templates from Bruzual & Charlot (2003) with a Chabrier (2003) initial mass function. We assume a delayed star formation history with an age (t) from 0.1 Gyr to the age of universe at the redshift of the galaxy in question and a star formation timescale parameter (τ) from 0.1 to 10 Gyr. Also the Calzetti et al. (2000) dust attenuation curve is assumed for internal extinction. The reddening parameter of $E(B-V)$ ranges from 0.0 to 1.5 with a step size of 0.025. The metallicity was allowed to have values of 0.2, 0.4, 1.0 and 2.5 $Z_\odot$. The SED fit returns the best fit parameters such as M_*, SFR, age, τ and $E(B-V)$. The SFR is defined as the averaged one over recent 100 Myr, based on the reasoning of Lee et al. (2009b). Figure 4 displays examples of SED fits for galaxies at $z \sim 1$. The solid line is the best fit SED, and points are observed fluxes at each band. The dotted line shows the SED in the top-left panel. For comparison purposes, we normalize the SEDs to the flux at observed frame 1.2 μm of each object.

The left panel in Figure 5 displays sSFR versus M_* of galaxies at $0.8 < z < 1.2$ in the SA22 field. We find that the fit of a power-law ($\log \mathrm{sSFR} = \alpha \log \mathrm{M}_* + \beta$) to the main sequence of star-forming galaxies has a slope of $\alpha = -0.33 \pm 0.03$ and an intercept of $\beta = -5.59 \pm 0.31$ (red line). For the estimation, we perform a double Gaussian fit to the sSFR distribution of galaxies in 5 different stellar mass bins from $M_* = 10^{10} M_\odot$ to $M_* = 10^{11.3} M_\odot$ with a width of 0.3 dex. Then the power-law is fit to the peak location of sSFRs for star-forming galaxies only. As a reference, the main sequence of star-forming galaxies at $0.8 < z < 1.2$ with the power-law slope of −0.10 from Elbaz et al. (2007) is displayed with a blue line. In addition, we also plot the main sequence of star-forming galaxies at $0.5 < z < 1.5$ taken from Wuyts et al. (2011) (green line), although the power-law slope of unity for the SFR–M_* relation was assumed in their analysis. On the other hand, Whitaker et al. (2012) suggested the significant evolution in the power-law slope of the SFR–M_* relation with redshifts. The relation at $z = 1$ derived by equations in Whitaker et al. (2012) is shown as an orange line with the slope of −0.43, which is similar to our estimate. We also note that our relation is similar to that in Whitaker et al. (2012), and our sample includes more high mass galaxies than Whitaker et al. (2012). This figure shows two loci of galaxies, one with $\log \mathrm{sSFR/yr}^{-1} > -10$, and another with $\log \mathrm{sSFR/yr}^{-1} < -10$.

Based on $J_{AB} < 23.2$ galaxies at $1.15 < z < 1.2$, the 80% percentile of the stellar mass distribution is $M_* \sim 10^{9.5} M_\odot$. However, we may miss a fraction of the lower mass, passive galaxies due to the relatively shallow optical data set. Therefore we use only galaxies more massive than $M_* = 10^{10} M_\odot$ for our analysis. The right panel in Figure 5 shows the stellar mass of detected galaxies as a function of redshift with $\log \mathrm{sSFR/yr}^{-1} < -10$ galaxies plotted in red and all other galaxies in black. The horizontal line is the stellar mass cut of $M_* = 10^{10} M_\odot$. Consequently, we extract 66,864 galaxies in $0.8 < z < 1.2$ with $M_* > 10^{10} M_\odot$ for this work.

3.2. Angular Two-point Correlation Function

One of the simplest ways to measure the clustering of galaxies is the two-point correlation function, which is the excess probability of finding a galaxy pair over a random distribution at a given scale (Peebles 1980). Here, we measure the angular two-point correlation function of galaxies at $0.8 < z < 1.2$, using the estimator introduced by Landy & Szalay (1993):

$$w_{\mathrm{obs}}(\theta) = \frac{DD(\theta) - 2DR(\theta) + RR(\theta)}{RR(\theta)}, \quad (1)$$

where DD is the number of galaxy pairs in $\theta \pm \Delta\theta$ in the observed data. In this work, the bin width is chosen as $\Delta \log \theta/\mathrm{degree} = 0.15$. DR and RR are the number of galaxy-random and random-random pairs, respectively. We generated 30 different random point catalogs having the same areal coverage and angular mask as observed with each random point catalog containing a similar number of random points to that of observed galaxies. The errors on the two-point correlation functions and the covariance matrices were estimated by the Jackknife resampling method, after splitting the UKIDSS DXS area into 48 sub-fields.

Although our data cover a wide area, it is hard to avoid the effect caused by the finite survey area, which is referred to as

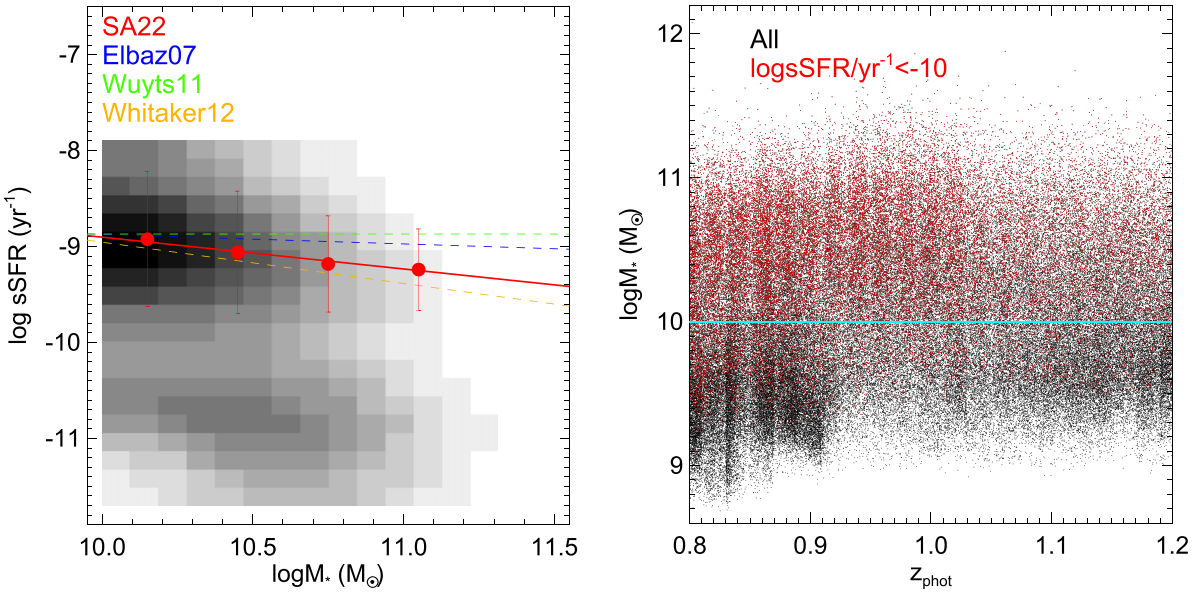

Figure 5. Left: the sSFR-stellar mass distribution of galaxies at $0.8 < z < 1.2$ in the SA22 field. The red line indicates the sSFR of the main sequence galaxies in this work. Red points present the peak location for star-forming galaxies derived by a double Gaussian fit to galaxies in different stellar mass bins (see the text for more details). The blue, green and orange lines are results from Elbaz et al. (2007), Wuyts et al. (2011) and Whitaker et al. (2012), respectively. Right: the stellar masses of galaxies in $0.8 < z_{\rm phot} < 1.2$. Black and red dots are all and log sSFR/yr$^{-1} < -10$ objects, respectively. The cyan line is the stellar mass cut ($M_* = 10^{10} M_\odot$) applied in this work. For the display purpose, objects in 1 deg^2 of surveyed area are plotted.

the integral constraint (IC, Groth & Peebles 1977) which is additive, i.e., $w(\theta) = w_{\rm obs}(\theta) + {\rm IC}$. This effect can be corrected by the empirical method in Roche et al. (1999) with an assumption of the actual shape of two-point correlation function. We apply two different approaches for stellar mass limited samples in Section 4 and sSFR binned samples in Section 5. For stellar mass limited samples, we use each two-point correlation function obtained from the halo model with observed parameters and then calculate the IC with the empirical equation in Roche et al. (1999). This process is included in the model fitting procedure to observed correlation functions, and taken into account to find the best fit HOD parameters (see Wake et al. 2011). However, the IC must be measured differently from stellar mass limited samples for sSFR binned samples, since we do not perform the halo modeling for this selection. As introduced in Kim et al. (2011), we assume the empirical functional form as the true correlation function, and then use the iterative method in Roche et al. (1999). In this work, we assume the functional form of $w(\theta) = \alpha_1 \theta^{-\beta_1} + \alpha_2 \exp(-\beta_2 \theta)$ (Kim et al. 2014). The combination of a power-law and an exponential component is necessary to describe small scale clustering of galaxies (power-law component) and large scale halo-to-halo clustering (exponential component), simultaneously. We note that the integral constraints of sub-samples range from 0.001 to 0.013 and that a more clustered sample tends to have a larger integral constraint value. Furthermore, for the stellar mass limited samples, the IC values measured by using the halo model and the functional form show the differences of <0.0017.

3.3. HOD Fit

Since galaxies reside in dark matter halos, the distribution of dark matter halos or density peaks are imprinted on the clustering of galaxies. In this context, we are able to link galaxies with dark matter halos through the halo model (see Cooray & Sheth 2002 for a review). Here, we apply a halo model using the HOD to study the relation between galaxies and their host dark matter halos. This model has been widely applied to various galaxy populations (Zheng et al. 2007; Blake et al. 2008; Wake et al. 2008; Ross & Brunner 2009a; Sawangwit et al. 2011; Wake et al. 2011; Zehavi et al. 2011; Krause et al. 2013; Nikoloudakis et al. 2013; Kim et al. 2014).

In order to model the best fit correlation function, we have to parameterize the basic components of the halo model such as the number density of halos, the satellite distribution in halos, the halo bias and the mean number of galaxies at a given halo mass. First, we adopt the halo mass function ($n(M_{\rm halo})$) and the halo bias function ($B(M_{\rm halo})$) from Tinker et al. (2010) for the number density and bias of halos, respectively. Second, the distribution of satellites is assumed to follow the NFW profile (Navarro et al. 1997) with the concentration parameter depending on redshift (Bullock et al. 2001; Zehavi et al. 2004; Blake et al. 2008; Ross & Brunner 2009a). Since $n(M_{\rm halo})$, $B(M_{\rm halo})$ and the NFW profile depend on redshift, we determine these at the mean redshift of our sample, i.e., $z = 1$. Finally, we specify the mean number of galaxies at a given halo mass ($N(M_{\rm halo})$), which in turn is parameterized for central galaxies ($N_{\rm c}$) and satellites ($N_{\rm s}$) separately and was introduced by Zheng et al. (2005), as

$$N(M_{\rm halo}) = N_{\rm c}(M_{\rm halo}) + N_{\rm s}(M_{\rm halo}), \quad (2)$$

with

$$N_{\rm c}(M_{\rm halo}) = 0.5\left[1 + {\rm erf}\left(\frac{\log_{10}(M_{\rm halo}/M_{\rm cut})}{\sigma_{\rm cut}}\right)\right] \quad (3)$$

and

$$N_s(M_{\rm halo}) = 0.5\left[1 + {\rm erf}\left(\frac{\log_{10}(M_{\rm halo}/M_{\rm cut})}{\sigma_{\rm cut}}\right)\right] \times \left(\frac{M_{\rm halo} - M_1}{M_0}\right)^{\alpha}, \quad (4)$$

where $M_{\rm halo}$ is a dark matter halo mass. $M_{\rm cut}$ and $\sigma_{\rm cut}$ define the transition halo mass and shape of HODs for central galaxies. M_1 is the truncation mass for satellites, and M_0 and α are the threshold halo mass and the slope for HODs of satellites, respectively (see also Zheng et al. 2005 and Wake et al. 2011).

Our survey area of $\sim 140h^{-1}$Mpc at $z = 1$ on one side is not wide enough to fully constrain all five free parameters ($M_{\rm cut}$, $\sigma_{\rm cut}$, M_0, M_1 and α) simultaneously. In previous work (Zheng et al. 2007; Brown et al. 2008; Zehavi et al. 2011), it was reported that M_1 is poorly constrained but similar to $M_{\rm cut}$ based on the SDSS data. Therefore we follow the relation, ($M_1 = M_{\rm cut}$), in this work. In addition, $M_{\rm cut}$ can be determined by matching the number density of galaxies with given parameters as applied in Ross & Brunner (2009a). Consequently, we have just three free parameters ($\sigma_{\rm cut}$, M_0 and α) to model the real-space correlation function.

We assume that the mean number of central galaxies is unity beyond a specific halo mass. Recent work based on cosmological simulations has argued that this can be below unity even in very massive halos due to active galactic nucleus (AGN) feedback (Kim et al. 2009; Gonzalez-Perez et al. 2011; Contreras et al. 2013), if the stellar mass threshold is chosen to be very large. However, the effect of AGN feedback is still controversial and there is a debate as to whether this is positive or negative on short timescales (<100 Myr). Therefore we do not consider this effect in this work. Furthermore, Zentner et al. (2013) pointed out that any halo model that does not take into account the assembly bias leads to a systematic error on the fitted result. Although this effect is significant for red populations, it is much reduced when considering all galaxies.

Using the basic components mentioned above, we follow the scheme of Ross & Brunner (2009a). Briefly, we model power spectra contributed by galaxies in the same halo (1-halo term) and in different halos (2-halo term). The 1-halo term is distinguished into central-satellite and satellite-satellite pairs again. In order to consider the underlying dark matter, the matter power spectrum is generated by the "CAMB" software package (Lewis et al. 2000) including the formulae of Smith et al. (2003) to model nonlinear growth. Then the modeled power spectrum is transformed to the real-space correlation function using the Limber Equation (LimXber 1954) to project the modeled real-space correlation function to angular space. The redshift distribution of each sub-sample is generated not by the best fit photometric redshift, but by the possible redshift distribution of each galaxy. We adopt 90% redshift ranges from the *Le Phare* software for each galaxy, then assume the Gaussian distribution above and below the redshift separately. This distribution of each galaxy is stacked to produce the redshift distribution. Finally, the modeled angular correlation function is fitted to the observed correlation function with the covariance matrix derived in Section 3.2 to find the best fit parameters. We fit the modeled correlation function to the observed one over the angular range $3\farcs2 < \theta < 0\fdg7$, where the influence of the IC is minimized.

Additionally, the effective halo mass ($M_{\rm eff}$), the effective bias (b_g) and the fraction of central galaxies ($f_{\rm cen}$) are derived from the best fit parameters with

$$M_{\rm eff} = \int dM_{\rm halo} M_{\rm halo} n(M_{\rm halo}) N(M_{\rm halo})/n_g, \quad (5)$$

$$b_{\rm g} = \int dM_{\rm halo} B(M_{\rm halo}) n(M_{\rm halo}) N(M_{\rm halo})/n_g \quad (6)$$

and

$$f_{\rm cen} = \int dM_{\rm halo} n(M_{\rm halo}) N_{\rm c}(M_{\rm halo})/n_g, \quad (7)$$

where n_g is the number density of galaxies, which is fixed to the observed value in this work.

We perform the halo modeling for only galaxies selected above a stellar mass threshold, since this model is appropriate for mass or luminosity limited samples. For the galaxies in stellar mass bins, the difference of HODs between two mass thresholds is calculated (see Section 4.2).

4. CLUSTERING WITH STELLAR MASS

In this section, we describe the results from fitting the halo model to galaxies split by different stellar mass thresholds of $M_* > 10^{10.0}, 10^{10.5}$ and $10^{11.0} M_\odot$ (Section 4.1). Then the HODs for galaxies in different stellar mass bins ($10^{10.0} M_\odot < M_* < 10^{10.5} M_\odot$, $10^{10.5} M_\odot < M_* < 10^{11.0} M_\odot$ and $M_* > 10^{11.0} M_\odot$) are compared in Section 4.2. Finally based on these HODs, the ratio between stellar mass and halo mass is discussed in Section 4.3.

4.1. Mass Threshold

In order to investigate the dependence of the HOD parameters on stellar mass, we split the selected galaxies at stellar mass thresholds of $M_* > 10^{10}$, $10^{10.5}$ and $10^{11} M_\odot$. In total, 66,864, 29,250 and 4564 galaxies are selected for each stellar mass threshold, respectively. The upper panels of Figure 6 show the measured angular two-point correlation function for each sub-sample (points with error bars). The relatively large error for $M > 10^{11.0} M_\odot$ comes from the significantly smaller number of galaxies. The solid line is the best fit halo model. As seen in Figure 6, the halo model reproduces the observed angular correlation function well. It also shows a relatively good fit even beyond the fitted range ($\theta > 0\fdg7$) and a more pronounced break between the 1- and 2-halo components as the balance of central to satellite galaxies changes with stellar mass. The best fit parameters and derived quantities are listed in Table 1.

The lower panels of Figure 6 display the best fit HODs for each sub-sample (solid line). The dotted and the dashed lines are HODs for central galaxies and satellites, respectively. It is clear that HODs for lower stellar mass galaxies extend down to a lower halo mass regime. This is well described by the best fit parameters of two halo mass thresholds ($M_{\rm cut}$ and M_0), which decrease for low mass galaxies. In addition, the HOD of more massive central galaxies shows a gentler transition shape compared to less massive central galaxies as already reported by Zehavi et al. (2011). The best fit parameter $\sigma_{\rm cut}$ describing the transition shape is 0.5 for $M_* > 10^{10} M_\odot$ and 0.6 for $M_* > 10^{11} M_\odot$. In order to check the effect of the galaxy number density to the best fit parameters, we perform the fit with four free parameters ($\sigma_{\rm cut}$, M_0, α and M_1). In this case, n_g

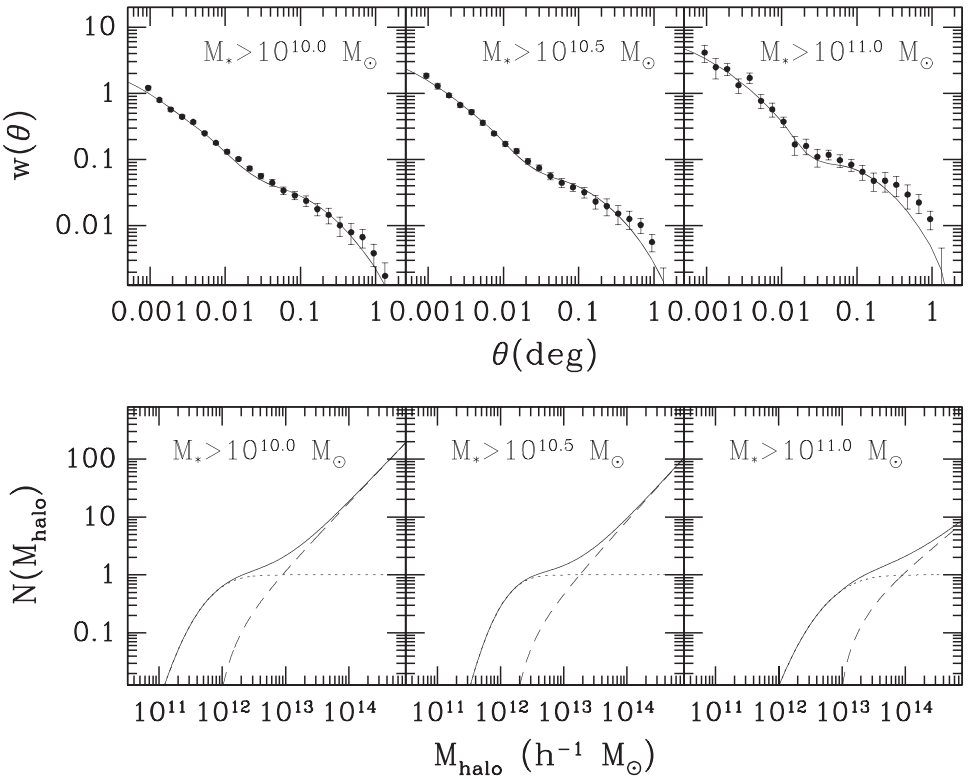

Figure 6. Upper panels show angular two-point correlation functions of galaxies selected by stellar mass thresholds indicated in each panel (points with error bars). The solid line is the best fit halo model. The lower panels present the best fit HODs (solid line). Dotted and dashed lines indicate HODs for central galaxies and satellites, respectively. It is clear that more massive galaxies are in more massive halos on average.

Table 1
The HOD Parameters for Stellar Mass Threshold Galaxies at $0.8 < z < 1.2$

Threshold (1)	$\sigma_{\rm cut}$ (2)	$M_{\rm cut}$ (3)	M_0 (4)	α (5)	n_g (6)	b_g (7)	$M_{\rm eff}$ (8)	$f_{\rm cen}$ (9)	χ^2/dof (10)
$10^{10.0}$	$0.50^{+0.02}_{-0.07}$	$11.885^{+0.036}_{-0.049}$	$12.912^{+0.011}_{-0.004}$	$1.14^{+0.03}_{-0.02}$	68.8	$1.62^{+0.04}_{-0.04}$	$12.778^{+0.041}_{-0.040}$	$0.84^{+0.01}_{-0.01}$	3.47
$10^{10.5}$	$0.40^{+0.03}_{-0.07}$	$12.163^{+0.046}_{-0.064}$	$13.215^{+0.015}_{-0.007}$	$1.20^{+0.04}_{-0.04}$	30.1	$1.83^{+0.07}_{-0.05}$	$12.892^{+0.053}_{-0.042}$	$0.87^{+0.01}_{-0.02}$	2.62
$10^{11.0}$	$0.60^{+0.04}_{-0.04}$	$12.958^{+0.060}_{-0.049}$	$13.909^{+0.039}_{-0.036}$	$0.90^{+0.05}_{-0.06}$	4.7	$2.25^{+0.08}_{-0.08}$	$13.117^{+0.038}_{-0.038}$	$0.94^{+0.02}_{-0.03}$	1.27

Note. Column (1) represents the stellar mass threshold for each sub-sample in $M_\odot$, columns (2–5) are the best fit HOD parameters and column (6) is the number density of galaxies in $10^{-4}h^3$ Mpc^{-3}. Columns (7–9) show the derived quantities base on Equations (5)–(7). The final column is the quality of the HOD fit in terms of χ^2 per degree of freedom. All dark matter halo masses are in $h^{-1}M_\odot$ with a logarithmic scale.

does not directly constrain M_1, but is calculated by the best fit parameters for matching the clustering only. Although, the parameters show different values from 3 parameter fits, the trend is exactly same. These results are presented in Appendix A.

Figure 7 shows derived quantities as a function of stellar mass thresholds with filled circles. The top and middle panels show the effective halo mass and the bias for each sub-sample. Clearly massive galaxies tend to reside in massive halos with high bias values, consistent with previous work. From the bottom panel of Figure 7, we can see that massive galaxies also tend to be the central galaxy in a massive halo.

Recently, many researchers have measured the clustering of galaxies split by stellar mass. For instance, Foucaud et al. (2010) measured the clustering of galaxies from the Palomar Observatory Wide-field Infrared Survey (Conselice et al. 2007). Their results show a halo mass of $\sim 10^{12.8}h^{-1}M_\odot$ and a bias of 1.9 for $10^{11}M_\odot < M_* < 10^{12}M_\odot$ galaxies at $0.8 < z < 1.2$, which is lower than ours (cross in Figure 7). However, their analysis was done over a 1.5 deg^2 area, which is >5 times smaller than ours. In addition, they measured halo masses based on the "one galaxy per halo" assumption with a correction for the halo occupation.

As mentioned above, HOD analysis may be affected by cosmic variance if the survey area is too small and the quality of the photometric redshifts used is poor. With these issues in mind we quote two more results, one from a much wider area and another one based on the spectroscopic information. First, Coupon et al. (2012) performed the halo modeling to reproduce the clustering of galaxies categorized by luminosity and type from the full CFHTLS–Wide survey area (~133 deg^2). Of our sub-samples, galaxies with $M_* > 10^{10.5}M_\odot$ and $10^{11.0}M_\odot$ have similar number densities to their sub-samples containing all galaxies at $M_g - 5\log h < -20.8$ and < -21.8 at $0.8 < z < 1.0$. Their estimates were $M_{\rm eff}$ of $10^{12.95}h^{-1}M_\odot$ and $10^{13.25}h^{-1}M_\odot$, bias of 1.74 and 2.25, and the satellite fraction ($f_{\rm sat}$) of 0.13 and 0.06 for $M_g - 5\log h < -20.8$ and < -21.8,

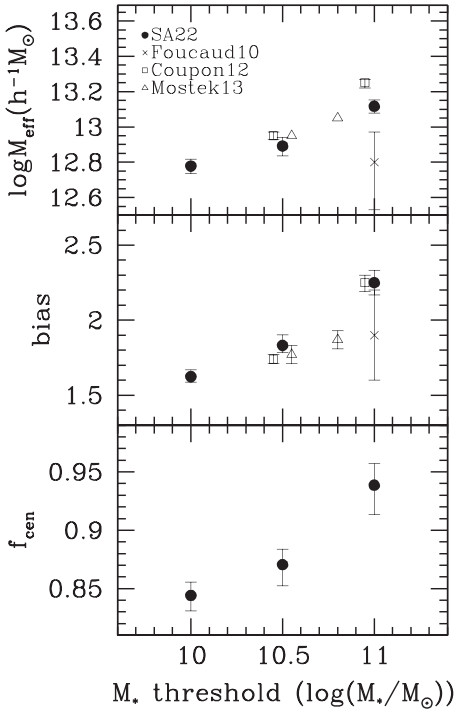

Figure 7. Derived effective halo masses (top), biases (middle) and fractions of central galaxies (bottom) from the halo modeling. More massive galaxies reside in more massive halos and tend to be central galaxies. As references, previous results from Foucaud et al. (2010), Coupon et al. (2012) and Mostek et al. (2013) are also displayed. For the display purpose, literature values are slightly shifted on the M_* axis.

respectively. Overall, these results are in good agreement with our estimates, although the halo mass for the brightest luminosity bin is about 0.15 dex higher than ours (open squares in Figure 7). Second, Mostek et al. (2013) used galaxies with spectroscopic information from the DEEP2 Galaxy Redshift Survey (Newman et al. 2013) to measure a projected correlation function of galaxies at $0.74 < z < 1.4$ at different stellar masses, SFRs and sSFRs. They estimated bias and mean halo mass as $(1.77,\ 10^{12.95}h^{-1}M_\odot)$ and $(1.87,\ 10^{13.05}h^{-1}M_\odot)$ for all galaxies at $0.74 < z < 1.05$ with $M_* > 10^{10.5}$ and $10^{10.8}M_\odot$, respectively (open triangles in Figure 7). Although the stellar mass thresholds are slightly different from our samples, all estimates are in good agreement with our values.

It is interesting to note that our estimates are consistent with CFHTLS (wide-area survey) and DEEP2 (a wide spectroscopic survey), while small area surveys give somewhat different results. Kim et al. (2011) demonstrated the importance of surveyed area for the reliable measurement of galaxy clustering on large scales in overcoming cosmic variance studying Extremely Red Objects. The scatter of clustering on large scales is ~30% and ~20% in areas of 0.26 and 0.6 $\deg^2$, respectively. In addition, the halo model with HODs may be a more reliable scheme to measure the masses of host halos for all, central and satellite galaxies, since this takes into account a more realistic contribution of central and satellite galaxies. Based on HODs discussed in this section, we can extend our analysis for galaxies split into stellar mass bins, which is an aspect that has not been fully explored in the literature.

4.2. Mass Bin

If we are able to find the HODs of galaxies in various stellar mass bins, we can understand the relation between galaxies and their host halos. However it is difficult to model the clustering of galaxies in stellar mass bins, since a different HOD shape should be assumed that is not well understood yet. In this section, we use the HODs discussed in Section 4.1 to obtain the HODs of galaxies in different stellar mass bins.

Zehavi et al. (2011) took the difference of HODs of luminosity threshold samples, in order to obtain the HODs of luminosity binned samples. We adopt this method to obtain the HODs of galaxies in different stellar mass bins. For instance, we obtain a HOD of galaxies at $10^{10.0}M_\odot < M_* < 10^{10.5}M_\odot$ by subtracting the HOD of $M_* > 10^{10.5}M_\odot$ galaxies from the HOD of $M_* > 10^{10}M_\odot$ galaxies. The bottom panels of Figure 8 show the HODs for $10^{10.0}M_\odot < M_* < 10^{10.5}M_\odot$ (left) and $10^{10.5}M_\odot < M_* < 10^{11.0}M_\odot$ (middle) galaxies, respectively, estimated in this way. For comparison, we also plot the HOD for $M_* > 10^{11.0}M_\odot$ galaxies in the right panel. The upper panels display the observed angular correlation functions (points) for each stellar mass binned sample. The solid lines in the top-left and top-middle panels are not the best fit results, but the modeled clustering based on the stellar mass binned HODs. The top-right panel is identical to that in Figure 6. The modeled correlation functions show a good agreement with the observed ones, except at a very small scales ($\theta \sim 0.^{\circ}001$) where the modeled correlation functions are slightly underestimated in comparison to the observed ones.

Returning to the HODs, we note that the HOD for central galaxies is similar to a log–normal distribution, which indicates that there is a crude correlation between the host halo mass and the stellar mass of the central galaxies (Moster et al. 2010). The width of the distribution reflects the amount of the scatter in this relation (Zheng et al. 2005), and we find that the central HOD for more massive galaxies covers a wider halo mass range at a given value of $N_c(M_{\rm halo})$ than that for less massive ones with the peak position shifted toward the high halo mass regime. As shown in the previous section, more massive galaxies show a gentler central HOD shape than less massive ones, which means a larger scatter between the stellar mass of central galaxies and the host halo mass. Therefore the broader shape of the HOD of massive galaxies reflects this effect. This can be caused by the stellar mass growth being stopped by any quenching mechanism, while the halos keep growing. For instance, Gonzalez-Perez et al. (2011) pointed out that the inclusion of AGN feedback leads to a change in slope and a larger scatter of the relation between K-band luminosities of central galaxies and their host halo masses, since the feedback presents gas cooling. In addition, Contreras et al. (2013) compared the HODs predicted by different semi-analytic models and show that the central HODs of more massive galaxies are more affected by this feedback in all simulations. The idea is that above a certain luminosity or mass, galaxies do not grow to have a very large stellar mass due to the negative feedback by AGN, resulting in cases where very massive halos possess central galaxies with reduced (but still massive) stellar masses. Consequently, the HOD of massive galaxies becomes extended toward a large halo mass.

The upper panel of Figure 9 shows the effective mass of dark matter halos hosting galaxies in each stellar mass bin calculated from the HODs. For the most massive bin, we plot the stellar

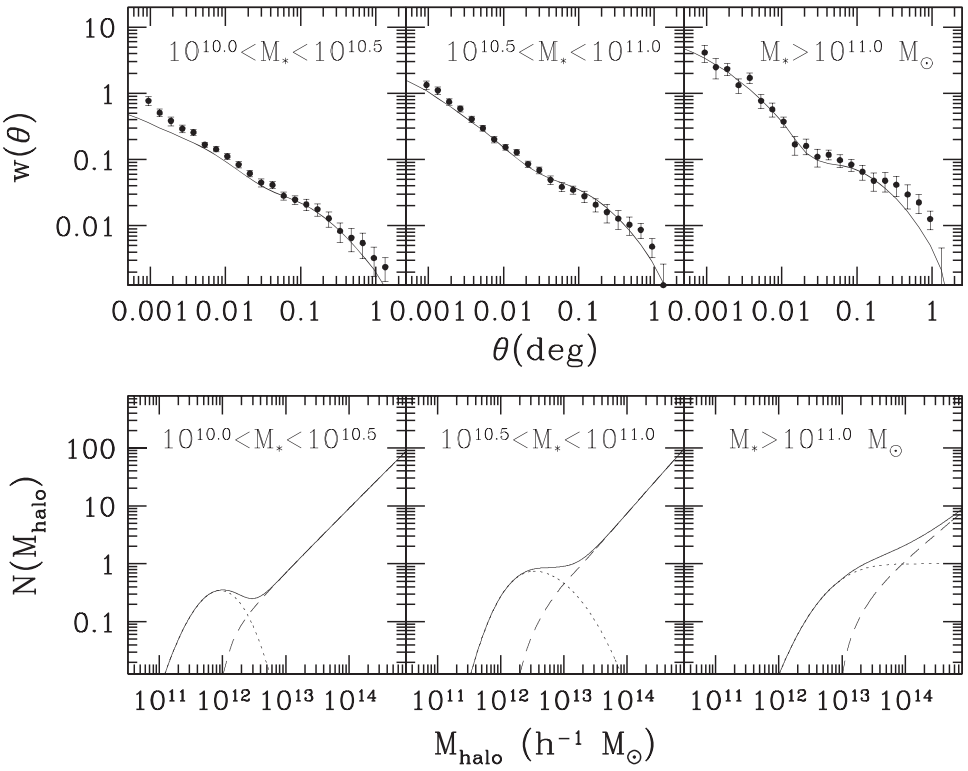

Figure 8. Similar plot as Figure 6 for stellar mass binned galaxies. All symbols are the same to Figure 6. However, the solid lines in the upper panel are reproduced angular correlation functions from the calculated HODs based on those for mass threshold galaxies (see text for more details). The most massive bin is identical to the right panel in Figure 6. More massive central galaxies are more widely distributed in halo masses than less massive ones.

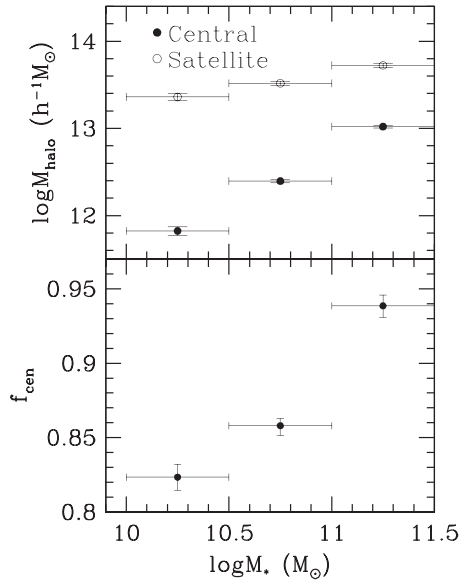

Figure 9. Upper panel shows the derived halo masses for central (filled circles) and satellite galaxies (open circles) in different stellar mass bins. The bottom panel represents the fraction of central galaxies. For the highest stellar mass bin, we use the $M_* > 10^{11} M_\odot$ galaxies. The horizontal bars indicate the size of stellar mass bins.

mass threshold sample of $M_* > 10^{11} M_\odot$. The mass of dark matter halos hosting central galaxies (filled circles) increases as the stellar mass increases with close to a linear slope. That for satellites (open circles) also shows a similar trend, but not as dramatic as it is for central galaxies. The reason for this difference in satellite galaxies is that a massive halo contains a large number of satellites in addition to a massive central galaxy. The bottom panel of Figure 9 displays the fraction of central galaxies in each stellar mass bin. This indicates that the massive galaxies are more likely to be central galaxies as the halo mass increases.

4.3. Stellar Mass to Halo Mass Ratio

Since galaxies evolve in dark matter halos, the properties of galaxies depend on their host dark matter halos. In this context, the relation between stellar mass (M_*) and halo mass ($M_{\rm halo}$) is a good testbed to constrain the evolution of galaxies. In addition, the ratio between the stellar mass of central galaxies and the halo mass is sensitive to the conversion efficiency from baryons to stellar mass in the central galaxy (Zheng et al. 2007). In previous work, the M_*–$M_{\rm halo}$ (or $M_*/M_{\rm halo}$–$M_{\rm halo}$) relation was derived using several different methods such as HOD, Conditional Luminosity Function and Sub-halo Abundance Matching (Zheng et al. 2007; Behroozi et al. 2010; Moster et al. 2010; Wang & Jing 2010; Wake et al. 2011). However, one of the advantages of the HOD framework is that the clustering and the number density of galaxies are fitted simultaneously without any assumption about the scatter between M_* and $M_{\rm halo}$ being a fixed value. Here, we derive the relation based on the best fit HODs directly, unlike previous HOD work, fitting a functional form to best fit HOD parameters.

We use the HODs for stellar mass binned samples discussed in the previous section to calculate the stellar mass to halo mass ratio ($M_*/M_{\rm halo}$). Since the HOD is the mean number of galaxies at a given halo mass, the summation of HODs multiplied by mean stellar masses for a given stellar mass bin

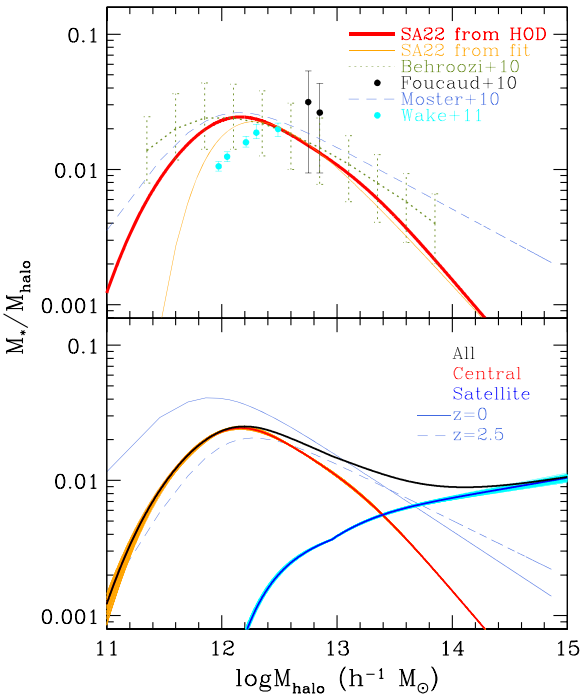

Figure 10. Stellar mass to halo mass ratio based on the best fit HODs. The upper panel is for central galaxies only at $z \sim 1$. The result of this work is represented by a thick red line. For comparison, we also plot previous results at $z \sim 1$ from Behroozi et al. (2010) (green dotted line), Foucaud et al. (2010) (black points), Moster et al. (2010) (blue short dashed line) and Wake et al. (2011) (cyan points). The ratio shows a peak at $\log M_{\rm halo} \sim 10^{12} h^{-1} M_\odot$, which is consistent with previous results. The orange line is the ratio calculated by the empirical function in Wake et al. (2011) for our result. The lower panel displays the ratio for central (red) and satellite (blue) galaxies. The black line is the combination of both central and satellite galaxies. The orange and cyan lines are results with varying HOD parameters randomly within the uncertainty range for central and satellite galaxies, respectively. Solid and dashed lines are from Moster et al. (2010) for $z = 0$ and 2.5 respectively. Satellites mainly contribute to the total stellar mass in group or cluster scale halos.

represents the stellar mass at a given halo mass. Therefore, the stellar mass at a given halo mass can be calculated by

$$M_*(M_{\rm halo}) = \sum N_i(M_{\rm halo}) \langle M_* \rangle_i \quad (8)$$

where $N_i(M_{\rm halo})$ is the central or satellite HOD for the ith stellar mass binned sample and $\langle M_* \rangle_i$ is the mean stellar mass of galaxies in the ith stellar mass bin. In this work, there are three stellar mass bins, each corresponding to $10^{10} M_\odot < M_* < 10^{10.5} M_\odot$, $10^{10.5} M_\odot < M_* < 10^{11.0} M_\odot$ and $M_* > 10^{11} M_\odot$. Using this stellar mass, we calculate the stellar mass to halo mass ratio.

The upper panel in Figure 10 shows the stellar mass to halo mass ratio for the central galaxy. The red solid line is the result based on Equation (8). The peak of the ratio is located at $\sim 10^{12.16} h^{-1} M_\odot$ with a ratio of 0.024. Below and above this halo mass, the ratio drops rapidly. This means that the conversion from baryons to stellar mass in the central galaxy is the most efficient in $\sim 10^{12} h^{-1} M_\odot$ dark matter halos as traced at $z \sim 1$. For the comparison, we also display the ratio at $z = 1$ (royal blue line) from Moster et al. (2010). We have to note that the ratio may be underestimated for low mass halos in this work, since the stellar mass limit is $M_* = 10^{10} M_\odot$, and less massive galaxies are missed. Therefore the actual slope of the ratio in the low halo mass regime may be flatter than our measurement.

Here, we also compare our result with other previous works. Wake et al. (2011) also performed the halo modeling for stellar mass limited samples from the NEWFIRM Medium Band Survey (Brammer et al. 2009; van Dokkum et al. 2009, 2010; Whitaker et al. 2011). After fitting the empirical function in Zehavi et al. (2011) to the best fit HOD parameters, they obtained the ratio at $z = 1.1$ (cyan points in Figure 10). Their result shows a peak at a higher halo mass, and a flatter (steeper) shape in a high (low) halo mass regime than ours, although the relation is poorly constrained at high and low halo masses. If we also fit the same function to our best fit parameters, this also shows a steeper slope in the low halo mass regime, but the discrepancy is not so significant in the high mass regime (orange line). On the one hand, this means that the functional form may underestimate the ratio for less massive halos, since this does not fully take into account HODs for stellar mass binned samples. On the other hand, for the high halo mass regime, the flatter trend may be caused by the different parameter set for HODs as Wake et al. (2011) fixed the transition shape of central HODs with $\sigma_{\rm cut} = 0.15$. In fact, the relation between derived halo mass parameters for central galaxies ($M_{\rm cut}$ in Equation (3)) and stellar masses in Wake et al. (2011) is flatter than ours. If we make the relation for our fitted parameters flatter arbitrarily, the ratio becomes much flatter in the high halo mass regime. Foucaud et al. (2010) also estimated the ratio as 0.032 ± 0.022 and 0.026 ± 0.017 for $10^{11} M_\odot < M_* < 10^{11.5} M_\odot$ and $10^{11.5} M_\odot < M_* < 10^{12.0} M_\odot$ at $0.8 < z < 1.2$, respectively (black points). Although these are in agreement within the uncertainty range, their halo masses are smaller compared to ours as mentioned above. Therefore it is possible that their points move toward a lower ratio and a higher halo mass regime, and become consistent with ours.

Additionally, Behroozi et al. (2010) obtained the same quantity using the abundance matching technique. We plot their result for the central galaxy including full uncertainties at $z = 1$ in the upper panel of Figure 10 (green points and line). Our result agrees with theirs within the uncertainty. However, our result may be slightly steeper in both the high and low halo mass regimes than the Behroozi et al. (2010) result. We find a similar discrepancy from Moster et al. (2010) as well (royal blue). As mentioned above, the ratio in the low halo mass regime is underestimated due to the stellar mass limit in this work. However, in the high halo mass regime, that is not the case and other factors may account for this discrepancy. First, Behroozi et al. (2010) and Moster et al. (2010) included the scatter in the M_*–$M_{\rm halo}$ relation with a fixed value. Whereas, our HOD takes into account such a scatter as shown in Figure 6. Behroozi et al. (2010) pointed out that a larger scatter in the relation makes the relation steeper. Second, the stellar mass uncertainty on individual galaxies can also affect the result, since the number of low mass galaxies having overestimated stellar masses is larger than that of high mass galaxies with underestimated stellar masses. If this scatter is included, the relation also becomes steeper (Behroozi et al. 2010).

In addition to the central galaxy, satellites also contribute to the total baryons in dark matter halos. Behroozi et al. (2010) and Foucaud et al. (2010) pointed out that satellites account for the majority of the total stellar mass in more massive dark matter halos. As we discussed in the previous section, satellite galaxies with $M_* > 10^{10} M_\odot$ tend to live in massive halos. The bottom panel in Figure 10 also shows this trend. The red line is the ratio for the central galaxy only, which is the same as in the

upper panel. The blue line is for satellites calculated by Equation (8) with the HODs in Figure 8. However, in this case, the value represents the ratio of the total stellar mass in satellites to the total mass of the dark matter halo. Orange and cyan lines are the results for central and satellite galaxies, respectively, which are derived from 100 different HOD sets with varying parameters ($\sigma_{\rm cut}$, M_1 and α) with values varied randomly within their measured uncertainty ranges. In contrast to the central galaxy, the ratio for satellites increases with increasing halo mass. In addition, the $M_*/M_{\rm halo}$ ratio for satellites is comparable with the value for the central galaxy in group environments ($10^{13}h^{-1}M_\odot < M_{\rm halo} < 10^{14}h^{-1}M_\odot$) and dominant in cluster environments ($M_{\rm halo} > 10^{14}h^{-1}M_\odot$). As discussed in Behroozi et al. (2010) and Foucaud et al. (2010), the accretion of dark matter toward a massive halo leads to the rapid growth of the halo mass. At the same time, infalling galaxies become satellites and contribute to the total stellar mass. However, the growth of central galaxies is not so efficient in this regime due to the deep potential well preventing an efficient merger or cold gas accretion onto the central galaxy. We also note that our data do not include faint, possibly numerous satellite galaxies. Thus, the $M_*/M_{\rm halo}$ ratio for satellites may be underestimated and can only be addressed with deeper data.

From the $M_*/M_{\rm halo}$ ratio for the central galaxy and satellites, we find that the star formation efficiency for the central galaxy is the most efficient in $\sim 10^{12}h^{-1}M_\odot$ dark matter halos at $z = 1$ with the $M_*/M_{\rm halo}$ ratio peaking at about 0.02. Moreover, we show that satellites are the dominant contributor to the $M_*/M_{\rm halo}$ of high mass halos ($M_{\rm halo} > 10^{13.5}h^{-1}M_\odot$). When we consider both central and satellite galaxy samples with $M_* > 10^{10}M_\odot$, we find the star formation efficiency in terms of total halo mass and stars in all galaxies is 1%–2% consistently. However, the cut–off at low halo mass is created by our selection of massive galaxies, so the mass of stars is not fully accounted for in the lowest mass halos. We also confirm the evolution of this relation, comparing to the result at different redshift from Moster et al. (2010) (the bottom panel in Figure 10).

5. CLUSTERING WITH STAR-FORMING ACTIVITY

The clustering of galaxies has been shown to depend on SFR and color. In this section, we split galaxies at $0.8 < z < 1.2$ based on their star-forming activity to investigate how their clustering properties depend on star formation. Additionally, since sSFR is roughly related to the star formation efficiency in a galaxy, we use various sSFR criteria to define each sub-sample.

5.1. Passive Versus Star-forming

We start with the comparison of bias values for different populations of galaxies. For this analysis, galaxies are split into passive and star-forming. In order to define the sSFR cut for passive galaxies, we check galaxies detected by *Spitzer* from the IRSA catalog.[8] We cross-match *Spitzer* sources to our galaxies with $M_* > 10^{10}M_\odot$ and $0.8 < z < 1.2$, and find 1871 IRAC and 213 24 μm sources. Of 24 μm sources, 15% and 8% satisfy log sSFR/yr$^{-1} < -10$ and -10.5, respectively. This means that the sSFR cut may not be a clean way to classify

[8] http://irsa.ipac.caltech.edu/applications/Gator/

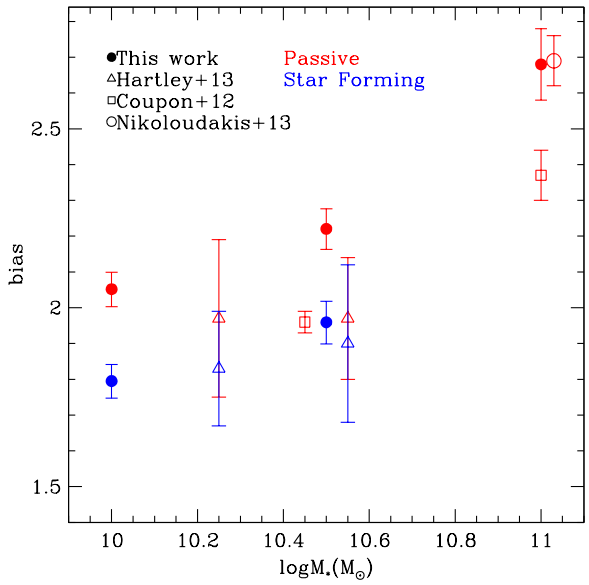

Figure 11. Biases for passive (red) and star-forming (blue) galaxies in $\log M_*/M_\odot > 10.0$, 10.5 and 11.0 (filled circles). Open triangles are from Hartley et al. (2013) with $10.0 < \log M_*/M_\odot < 10.5$ and $\log M_*/M_\odot > 10.5$. Open squares are for red galaxies in Coupon et al. (2012) with $M_g - 5\log h < -20.8$ and -21.8. Also the open circle shows the result of LRGs at $z \sim 1$ in Nikoloudakis et al. (2013). For the display purpose, open symbols are slightly shifted along the M_* axis.

pure passive galaxies, but we can isolate them efficiently. Thus, although there are two galaxy loci in Figure 5 separated by log sSFR/yr$^{-1} \sim -10$, we classify passive galaxies with log sSFR/yr$^{-1} < -10.5$ in order to minimize the contamination by dusty galaxies. Then, star-forming galaxies are defined by log sSFR/yr$^{-1} > -10$. we then apply stellar mass cuts with $M_* > 10^{10.0}$, $10^{10.5}$ and $10^{11.0}M_\odot$ for each population. However, since the number of star-forming galaxies in the highest mass bin is too small to measure the clustering, we do not include this sub-sample in our analysis.

For each selected sub-sample, the angular two-point correlation function is measured. Since the intrinsic HOD shape for each sample is not well understood, we estimate the bias by fitting the angular correlation function of the underlying dark matter instead of finding the best fit HODs. First, we obtain the real space correlation function of dark matter from the linear matter power spectrum at $z = 1$. Then the real space correlation function is transformed into the angular correlation function with the observed redshift distribution, after multiplying it by the bias value. Through fitting the transformed angular correlation function to the observed one, we find the best fit bias values for each sub-sample. The fitting is performed to the angular range between $0\overset{\circ}{.}02$ and $0\overset{\circ}{.}7$, where the influence by the IC is minimized and 2-halo component dominates.

Filled circles in Figure 11 show the estimated bias for passive (red) and star-forming (blue) galaxies. It is clear that passive galaxies are more clustered than star-forming ones, which is consistent with previous results at the similar redshift (Coil et al. 2008; McCracken et al. 2008; Williams et al. 2009; Hartley et al. 2010, 2013; Bielby et al. 2014). Additionally, high mass galaxies show a stronger clustering strength than low mass ones independently of population. On the other hand, some previous results pointed out that passive or red galaxies

show similar (or higher) clustering strengths with decreasing stellar masses (DEEP2 in Coil et al. 2008 and UKIDSS UDS in Williams et al. 2009 and Hartley et al. 2013). Open triangles in Figure 11 are for galaxies with $10^{10}M_{\odot} < M_{*} < 10^{10.5}M_{\odot}$ and $M_{*} > 10^{10.5}M_{\odot}$ at $z \sim 1.06$ from Hartley et al. (2013) based on the UKIDSS UDS data. Passive galaxies show a similar clustering strength in both bins, which implies that there is no stellar mass dependence. This was interpreted as the contribution of low mass satellite galaxies in massive halos, leading to similar clustering strengths independently of the stellar mass.

Our results may appear to be different from previous literature results. However, we also display bias values for red galaxies with $M_g - 5\log h < -20.8$ and -21.8 (red open square) at $0.8 < z < 1.0$ from CFHTLS in Coupon et al. (2012). The number densities in each magnitude bin are similar to those for our passive galaxies with $M_{*} > 10^{10.5}$ and $10^{11}M_{\odot}$, respectively. Although their measurements are lower than ours, brighter red galaxies are more clustered than fainter ones, which is the same trend to our passive galaxies. Possibly lower values are caused by different selection criteria, since absolute magnitude limited samples can include low stellar mass galaxies, but exclude some high mass ones. In addition, they noted that red galaxies at $z > 0.8$ were contaminated by blue galaxies. The similar trend was also found in McCracken et al. (2008), which showed early-type galaxies with brighter absolute magnitude are more strongly clustered than fainter early-type galaxies at $0.7 < z < 1.1$, based on the CFHTLS data. Finally, we also note the bias value from LRGs at $z \sim 1$ from Nikoloudakis et al. (2013) (red open circle). The number density of LRGs in their paper is similar to that of our high mass passive galaxies, and the estimated bias is also consistent.

Since the area coverage of our data is not wide enough to fully overcome the effect of cosmic variance, it may be hard to conclude whether the clustering strength of passive galaxies at $z \sim 1$ is correlated with stellar mass in our data set conclusively. However, our result shows the consistent trend with the result from the wider survey data, which indicates our data set is not significantly affected by cosmic variance. Based on this conclusion, we investigate the clustering property of galaxies with finer sSFR bins below.

5.2. sSFR bins

As shown in Section 3.1.2, the main sequence of star-forming galaxies has a slope of −0.33 on the sSFR versus stellar mass plane. However, our main goal is to investigate the clustering strength as a function of star formation activities at $z \sim 1$. Thus, we simply apply five sSFR bins for star-forming galaxies ($-8.5 <$ log sSFR/yr^{-1} < -8.0, $-8.85 <$ log sSFR/yr^{-1} < -8.5, $-9.25 <$ log sSFR/yr^{-1} < -8.85, $-9.7 <$ log sSFR/yr^{-1} < -9.25 and $-10.1 <$ log sSFR/yr^{-1} < -9.7). The width of each bin is determined to include sufficient galaxies for a reasonable clustering measurement. Additionally, passive galaxies are defined as galaxies with log sSFR/yr^{-1} < -10.5, and they are further divided into mass thresholds of $M_{*} > 10^{10}$, $10^{10.5}$ and $10^{11}M_{\odot}$. Column 3 in Table 2 lists the number of galaxies in each bin. We also compare the clustering properties in each sSFR bin with narrower stellar mass bins later.

Figure 12 displays the angular correlation function of each sub-sample (points) and the best fit result (solid line). The top three panels are for passive galaxies with different stellar mass thresholds. The second and third rows are results for star-forming galaxies in various sSFR bins with $M_{*} > 10^{10}M_{\odot}$. The labels in the second and third rows indicate the sSFR range in a logarithmic scale. We also plot the best fit result for $M_{*} > 10^{11}M_{\odot}$ passive galaxies with dotted line. After comparing the solid and the dotted lines for sSFR binned samples, the difference is the largest for $-8.85 <$ log sSFR/yr^{-1} < -8.5 galaxies, which means it has the lowest bias among our sub-samples. On small scales, we are able to find excess of clustering amplitudes from all sub-samples, although the measurement with relatively large uncertainties is affected by the small number of objects. However, the excess for star-forming galaxies looks less significant than passive ones. This may mean that the number of star-forming satellites in each bin is lower than passive satellites, which intrinsically weakens the clustering strength. However, the actual spatial distribution of satellites in each sub-sample may also influence the clustering. For an extreme example, if a star-forming sub-sample includes one satellite per halo and just a portion of centrals, the small scale clustering is more weakened than the large scale. Unfortunately, our data is not enough in depth and area to demonstrate these effects separately (or simultaneously). Larger and deeper data sets in the future will allow us to investigate this issue. In this work, we will focus on the bias or halo mass estimated from the large scale clustering only.

Table 2
Results for sSFR Binned Galaxies with Stellar Mass Thresholds

M_{*} (1)	sSFR range (2)	$N_{\rm gal}$ (3)	Bias (4)	$M_{\rm halo}$ (5)
$M_{*} > 10^{10}$	−8.50 to −8.00	6387	$2.01^{+0.08}_{-0.07}$	$12.785^{+0.064}_{-0.057}$
	−8.85 to −8.50	9219	$1.89^{+0.07}_{-0.07}$	$12.684^{+0.064}_{-0.061}$
	−9.25 to −8.85	9089	$2.39^{+0.09}_{-0.09}$	$13.048^{+0.056}_{-0.055}$
	−9.70 to −9.25	6526	$2.38^{+0.11}_{-0.11}$	$13.041^{+0.069}_{-0.067}$
	−10. to −9.70	4101	$2.51^{+0.11}_{-0.12}$	$13.121^{+0.064}_{-0.062}$
	<−10.5	24,958	$2.05^{+0.05}_{-0.05}$	$12.817^{+0.038}_{-0.037}$
$M_{*} > 10^{10.5}$	<−10.5	15,863	$2.22^{+0.06}_{-0.06}$	$12.940^{+0.039}_{-0.038}$
$M_{*} > 10^{11.0}$	<−10.5	3583	$2.68^{+0.10}_{-0.11}$	$13.207^{+0.053}_{-0.052}$

Note. Column (1) is the stellar mass threshold in $M_{\odot}$, column (2) shows the sSFR range with a logarithmic scale in yr^{-1} and column (3) is the number of galaxies in each bin. Columns (4–5) are the measured bias and the estimated halo mass, respectively. The unit of halo masses is in $h^{-1}M_{\odot}$.

Figure 13 shows the estimated bias as a function of sSFR (points). The size of the points for passive galaxies represents the stellar mass thresholds which are $M_{*} > 10^{10}$, $10^{10.5}$ and $10^{11}M_{\odot}$ from small to large points, respectively. For star-forming galaxies, a single mass threshold of $M_{*} > 10^{10}M_{\odot}$ is applied. For comparison, we also plot the result of blue galaxies with $M_B < -20.5$ at $0.74 < z < 1.05$ from Mostek et al. (2013) (open squares). As found by Mostek et al. (2013), we also confirm that the bias or a clustering strength decreases with increasing sSFRs up to log sSFR/yr^{-1} ~ -8.6. The discrepancy of biases may come from different selection criteria, since they have used rest-frame magnitude limited samples that may include $M < 10^{10}M_{\odot}$ galaxies which can dilute their measured clustering strength. Since the sSFR value for the main sequence at $z = 1$ is log sSFR/yr^{-1} ~ -9 in Figure 5, galaxies just above (or the upper part of) the main sequence show the lowest bias, which is consistent with

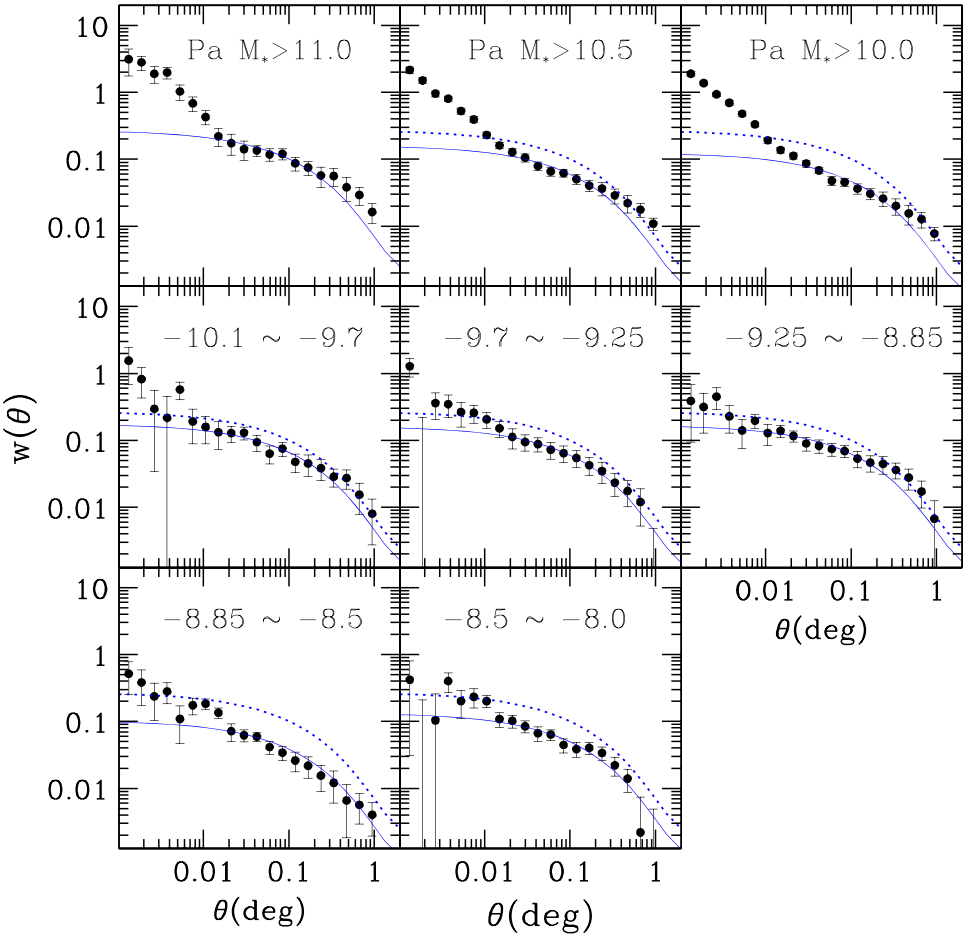

Figure 12. Angular correlation functions (points) for sSFR binned samples. The top row is for passive galaxies (log sSFR/yr^{-1} < −10.5) with different stellar mass thresholds. The middle and bottom rows are for star-forming galaxies in various sSFR bins as labeled. The solid line is the best fit result, and the dotted line is for $M_* > 10^{11}M_\odot$ passive galaxies. Comparing solid and dotted lines, the amplitude difference is the largest in the bottom-left panel, which indicates the lowest bias.

Mostek et al. (2013). This anti-correlation has been reported at $z \sim 1$ by Coil et al. (2008) and Mostek et al. (2013), and in the local universe by Li et al. (2008) and Heinis et al. (2009). However, we also see a possible reversal of the relation in the highest sSFR bin ($-8.5 <$ log sSFR/yr$^{-1} < -8.0$).This was already noted by Lin et al. (2012) for sBzK galaxies at $z \sim 2$, but we find a similar trend at $z \sim 1$ and we plot their results with open triangles. Direct comparison of the absolute values is difficult due to different stellar mass limits. Galaxies in this work are more massive than those in Lin et al. (2012). However, both results show the same trend, and we find a similar sSFR for the lowest bias sample.

Additionally, we note the mass of halos hosting each subsample. The halo mass is calculated using the measured bias and the halo mass function in Tinker et al. (2010). Since this procedure does not consider the inclusion of satellites, the calculated halo mass may show a discrepancy from that from the full HOD framework in previous sections. However, since our main goal here is to examine how the bias factor or host halo mass change as a function of sSFR, we will defer an HOD analysis to a future paper where we will include more galaxies over a wider area. Details of the influence of satellites are well described in Zheng et al. (2007). In Appendix B, we also compare halo masses derived by the halo model and the direct fit. Our measured biases and halo masses are given in Table 2. We find that the mass of host halos of galaxies with the lowest bias is $M_{\rm halo} = 10^{12.684}h^{-1}M_\odot$. Also the mean halo masses for passive galaxies are $M_{\rm halo} = 10^{12.817}, 10^{12.940}$ and $10^{13.207}h^{-1}M_\odot$ from the lowest to the highest stellar mass bins, respectively.

From Figure 13, we show the clustering strength as a function of sSFRs. Now we investigate the same quantities using galaxies in different stellar mass bins, in order to check the influence of stellar mass as the negative main sequence slope on the sSFR–mass plane could arise from a selection bias toward high sSFR galaxies that are in less massive halos and hence are less clustered. To assess the level of this potential bias we further split galaxies into different stellar mass bins of $10^{10}M_\odot < M_* < 10^{10.5}M_\odot$ (LM) and $10^{10.5}M_\odot < M_* < 10^{11}M_\odot$ (HM) with the same sSFR bins mentioned above. Unfortunately, it is hard to measure the secure angular correlation function of star-forming galaxies with $M_* > 10^{11}M_\odot$ divided into various sSFR bins because of the small number of objects. Thus, we do not consider the highest stellar mass bin here. Figure 14 shows the observed correlation function of sSFR binned samples in LM (blue) and HM (red). Symbols are the same as Figure 12. Black labels indicate sSFR ranges. As already shown in Section 5.1, passive galaxies in HM is more clustered than those in LM. On the other hand, star-forming galaxies with log sSFR $\lesssim -9$ in LM show stronger clustering strengths than HM ones, but this is opposite at the high sSFR range.

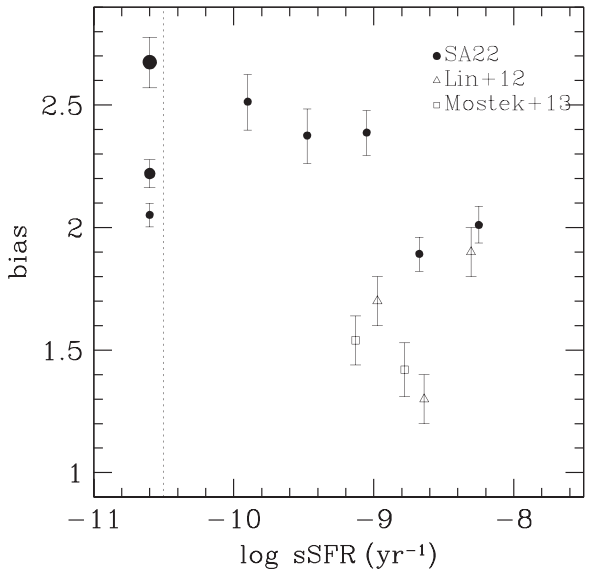

Figure 13. Bias of sSFR binned galaxies. The vertical dotted line shows the criterion distinguishing star forming and passive galaxies. For passive galaxies (log sSFR/yr^{-1} < −10.5), a symbol size corresponds to stellar mass thresholds, $M_* > 10^{10}$, $10^{10.5}$ and $10^{11}M_\odot$ from small to large points. The previous results for $z \sim 2$ sBzKs (Lin et al. 2012) and $z \sim 1$ galaxies (Mostek et al. 2013) are also plotted with open triangles and open squares, respectively. The clustering strengths increase with decreasing sSFRs. However, it is also found that the highest sSFR galaxies are more strongly clustered than main sequence galaxies.

Figure 15 displays the halo mass as a function of sSFR for the $10^{10}M_\odot < M_* < 10^{10.5}M_\odot$ (blue) and $10^{10.5}M_\odot < M_* < 10^{11}M_\odot$ (red) bins, respectively. In this case, we plot the halo mass on the y-axis rather than the bias factor. From both stellar mass bins, we confirm the anti-correlation in the sSFR–$M_{\rm halo}$ relation in the low sSFR regime of star-forming galaxies and at lower significance the reversal of the relation at log sSFR/yr^{-1} > −8.5 shown in Figure 13. This means that the feature shown in Figure 13 is mainly caused by an environmental effect connecting the halo occupation of high sSFR galaxies to the mass of their host halo and not due to an effect intrinsic to their stellar mass. One difference between two mass bins is the sSFR value showing the lowest halo mass. Although the uncertainty is substantial, HM star-forming galaxies with the lowest halo mass have lower sSFR than LM ones. Considering the slope for main sequence galaxies in Figure 5, galaxies on the upper envelope of the main sequence in each stellar mass bin reside in the lowest mass halos. The number of galaxies in each bin and all the measured values are listed in Table 3.

Finally, it is worth comparing our results to the known sSFR–local density relation. First, Cooper et al. (2008) found the same anti-correlation at $z \sim 1$ over the similar sSFR range from the DEEP2 survey. In addition, we can also see a suggestion of a weak reverse relation in the highest sSFR bin (see Figure 9 in their paper). Second, Ko et al. (2012) also reported the similar trend at $z = 0.087$ based on the AKARI North Ecliptic Pole Wide survey and A2255 from the AKARI CLusters of galaxies EVoLution studies (Im et al. 2008; Lee et al. 2009a). Although Ko et al. (2012) focused on the very low redshift, there is no significant difference in the bias–sSFR relations at low and high redshifts as we already mentioned above. Moreover, their field coverage is wide enough to study the relation from low to high local densities. In conclusion, our results also show good agreement with local density studies.

6. DISCUSSION

In the previous section, we found a clear dependence of clustering strength on sSFR. Here, we further investigate the property of galaxies in the highest sSFR bin, which are in denser environments than main sequence star-forming galaxies, and we present a possible scenario for the evolution of star-forming galaxies.

We begin with the comparison of the internal dust attenuation of $E(B-V)$ derived from SED fitting. The top panel of Figure 16 shows the $E(B-V)$ distribution of the highest sSFR galaxies (−8.5 < log sSFR/yr^{-1} < −8.0) and the main sequence galaxies (−9.5 < log sSFR/yr^{-1} < −8.5) with solid and dotted histograms, respectively. In addition, galaxies are also split into two stellar mass bins of $10^{10} < M_*/M_\odot < 10^{10.5}$ (blue) and $M_* > 10^{10.5}M_\odot$ (red). The inset shows the cumulative distribution of each sub-sample. The median values of $E(B-V)$ for the highest sSFR bin is 0.45 and 0.55 for $10^{10} < M_*/M_\odot < 10^{10.5}$ and $M_* > 10^{10.5}M_\odot$ galaxies, respectively. However, those for main sequence galaxies in the same stellar mass bins are 0.375 and 0.45, respectively. It is clear that high sSFR galaxies are more heavily obscured at a given stellar mass and in strongly biased regions than the main sequence galaxies. Whitaker et al. (2012) categorized high sSFR galaxies as dusty, blue star-forming galaxies, and noted that they are possibly merger driven starburst galaxies. We also show in Figure 16 the distribution of $g-J$ color (bottom) corresponding to the rest-frame UV–optical color. The line styles are the same as the top panel. This bluer color is also confirmed by the best fit SED in Figure 4. The bottom panels in Figure 4 are examples of high sSFR galaxies. Compared to main sequence galaxies (middle panels in Figure 4), it is clear that high sSFR galaxies show significantly higher fluxes in the rest-frame UV regime. Although there is a significant overlap, high sSFR galaxies are either relatively blue $g-J$ color or have a higher extinction suggesting the presence of an obscured young stellar population.

Although these high sSFR galaxies are most likely to be obscured galaxies with efficient star formation, their colors could also be strongly affected by the presence of an AGN. From the previous work based on the clustering, AGN reside in dark matter halos of $>10^{13}h^{-1}M_\odot$ (e.g., Hickox et al. 2009, 2011; Ross et al. 2009b; also see a review in Cappelluti et al. 2012 and references therein). Interestingly, this halo mass is consistent to our result for high sSFR galaxies. Therefore, in order to test the possibility of AGN contamination, we check the fraction of AGN in this high sSFR bin. Using *Spitzer* sources mentioned above, we select 75 potential AGN with IRAC colors suggested by Stern et al. (2005). Among these AGN, 15 sources are in the highest sSFR bin, and this corresponds to ∼8.8% of all IRAC sources matched with our galaxies in the same sSFR bin. In addition to *Spitzer* data, we also select potential AGN in the whole studied area from the *Wide–field Infrared Survey Explorer* (*WISE*) with a simple color cut suggested by Stern et al. (2012). Although the depth of *WISE* data is not enough to detect faint AGN, the wide area is helpful to measure the clustering after excluding bright AGN. We remove potential *WISE* AGN from our high sSFR

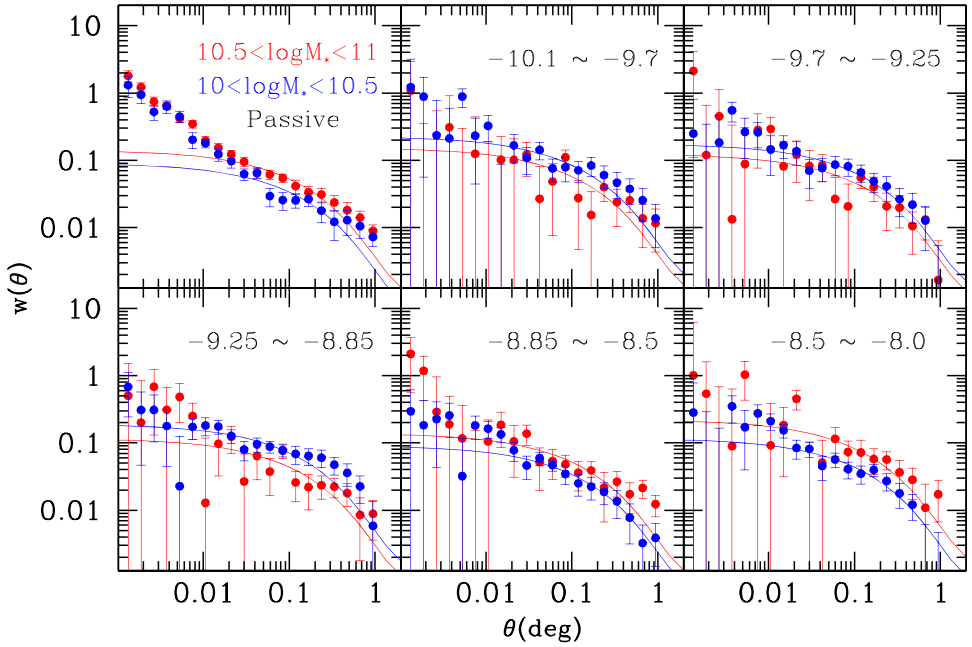

Figure 14. Angular correlation functions for sSFR binned samples in $10^{10} < M_*/M_\odot < 10^{10.5}$ (blue) and $10^{10.5} < M_*/M_\odot < 10^{11}$ (red). Points with error bars are correlation functions measured and solid lines are the best fit dark matter clustering on large scales. Black labels in each panel indicate the sSFR range in a logarithmic scale.

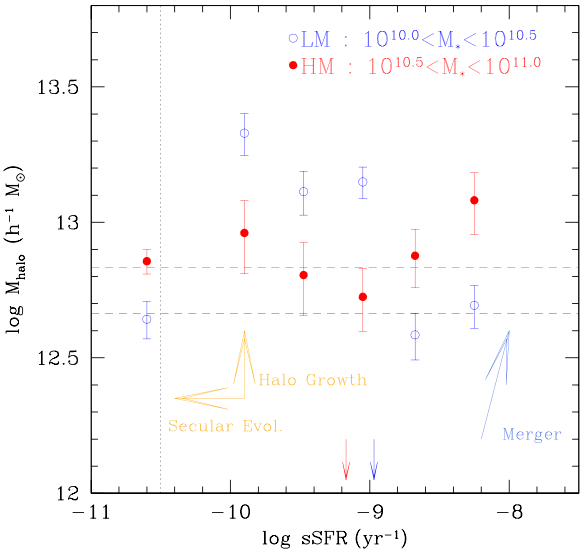

Figure 15. Similar plot to Figure 13 for $10^{10}M_\odot < M_* < 10^{10.5}M_\odot$ (blue open circle) and $10^{10.5}M_\odot < M_* < 10^{11}M_\odot$ (red filled circle) galaxies. In this plot, we quote calculated halo masses instead of bias values. We confirm the trend in Figure 13 from narrower stellar mass binned samples. The arrows present possible evolutionary paths. See text for more details and discussion. The horizontal dashed lines indicate $M_{\rm eff}$ values of halos for all galaxies in each stellar mass bin. Downward arrows at the bottom are central sSFR values of the main sequence for each stellar mass bin.

galaxies, and then measure the clustering again. The fractions of galaxies excluded are 3.6% in the LM bin and 8.9% in the HM bin. The re-measured clusterings are identical to those for the previous measurements in both bins. Since the triggering mechanism for AGN is not well understood yet, we cannot rule out the connection between high sSFR galaxies and AGN. However, our result for the highest sSFR bin is not biased by AGN.

Table 3
The Same Table with Table 2, But for Stellar Mass Binned Galaxies

M_* (1)	sSFR range (2)	$N_{\rm gal}$ (3)	Bias (4)	$M_{\rm halo}$ (5)
$10^{10} < M_* < 10^{10.5}$	−8.50 to −8.00	5082	$1.90^{+0.09}_{-0.09}$	$12.694^{+0.081}_{-0.077}$
(LM)	−8.85 to −8.50	6675	$1.79^{+0.08}_{-0.09}$	$12.585^{+0.089}_{-0.083}$
	−9.25 to −8.85	6100	$2.56^{+0.10}_{-0.11}$	$13.149^{+0.059}_{-0.057}$
	−9.70 to −9.25	4049	$2.50^{+0.14}_{-0.15}$	$13.114^{+0.082}_{-0.079}$
	−10.1 to −9.70	2394	$2.93^{+0.17}_{-0.18}$	$13.329^{+0.079}_{-0.075}$
	< −10.5	9095	$1.85^{+0.07}_{-0.08}$	$12.643^{+0.070}_{-0.067}$
$10^{10.5} < M_* < 10^{11}$	−8.50 to −8.00	1257	$2.44^{+0.18}_{-0.20}$	$13.081^{+0.115}_{-0.109}$
(HM)	−8.85 to −8.50	2418	$2.13^{+0.14}_{-0.15}$	$12.877^{+0.110}_{-0.103}$
	−9.25 to −8.85	2807	$1.94^{+0.13}_{-0.14}$	$12.725^{+0.119}_{-0.110}$
	−9.70 to −9.25	2260	$2.04^{+0.16}_{-0.18}$	$12.806^{+0.138}_{-0.127}$
	−10.1 to −9.70	1527	$2.25^{+0.19}_{-0.21}$	$12.961^{+0.137}_{-0.127}$
	< −10.5	12280	$2.10^{+0.06}_{-0.06}$	$12.857^{+0.046}_{-0.045}$

Note. Column (1) represents the stellar mass range.

Above, we noted that galaxies with the highest sSFR reside in more massive halos than main sequence galaxies. There are numerous reports in the literature that the star formation activity is enhanced by merger or the tidal interaction of galaxies (Mihos et al. 1992; Barton et al. 2000; Lambas et al. 2003; Ellison et al. 2008; Hwang et al. 2011; Ideue et al. 2012; Kampczyk et al. 2013; Patton et al. 2013). Daddi et al. (2010) and Genzel et al. (2010) also reported that starburst galaxies driven by mergers form stars more efficiently than normal star-forming galaxies. Furthermore, it has been thought that these processes more easily occur in dense environments such as galaxy groups (McIntosh et al. 2008; Perez et al. 2009; Pipino et al. 2014). So when combined with the observation that these galaxies are dustier and form stars efficiently, it suggests that high sSFR galaxies can be generated by mergers or interaction. Also, since massive galaxies usually

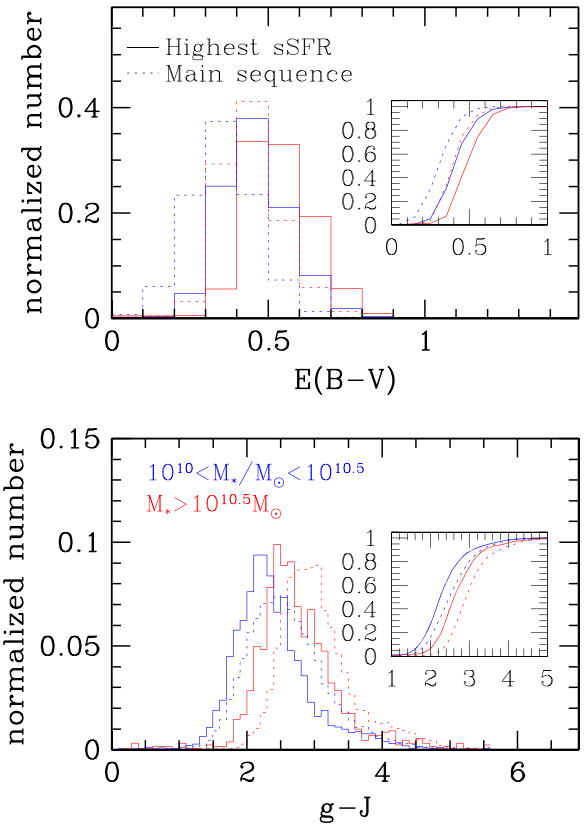

Figure 16. $E(B-V)$ (top) and $g-J$ color (bottom) distributions of galaxies with $10^{10} < M_*/M_\odot < 10^{10.5}$ (blue) and $M_* > 10^{10.5} M_\odot$ (red). Solid and dotted histograms are for the highest sSFR galaxies ($-8.5 <$ log sSFR/yr$^{-1} < -8$) and main sequence ones ($-9.5 <$ log sSFR/yr$^{-1} < -8.5$), respectively. The inset shows the cumulative distribution with the same line style to the main panel. The highest sSFR galaxies are more heavily obscured and show relatively bluer colors than main sequence galaxies at a given stellar mass.

reside in massive halos, high sSFR HM galaxies experience the processes in massive halos imprinting the ∼0.4 dex high halo mass compared to high sSFR LM galaxies as seen in Figure 15. This is consistent with Lin et al. (2012) who speculated that galaxies with the highest sSFR might be linked to mergers or interactions in halos more massive than those hosting main sequence galaxies. Another possible explanation for high sSFR galaxies is that they are primarily in massive halos like galaxy with enhanced star formation at $z \sim 2$. Magliocchetti et al. (2014) pointed out that galaxies forming stars actively at $z \sim 2$ are a different population from similar objects at $z < 1$, based on the comparison of clustering strengths. They reported the halo mass of $>10^{13} M_\odot$, and they evolve into passive galaxies at $z < 1.5$. The halo mass is consistent with that for our high sSFR samples. Moreover, Popesso et al. (2015) also find that most IR-luminous galaxies at $z > 1$ reside in the group environment, which is also similar to that for our high sSFR galaxies. In this sense, our high sSFR galaxies may be in the transition phase experiencing a rapid evolution to a passive population.

Now, we recall the HODs in Figure 8 to interpret Figure 15. First, we briefly note the halo mass difference measured by the halo model and the fit of dark matter clustering, since we directly estimate the bias with the dark matter clustering for sSFR binned samples. As we discuss in Appendix B, the halo mass from the dark matter clustering fit is between representative halo masses for central and satellite galaxies from the halo model. If there are more satellites, this becomes closer to that for satellites. Furthermore, $M_{\rm eff}$ of dark matter halos from the halo model is more significantly influenced by satellites. In Figure 15, the horizontal dashed lines are $M_{\rm eff}$ values for all galaxies in each stellar mass bin.

For LM galaxies, $M_{\rm eff}$ for all galaxies from the halo model is $10^{12.66} h^{-1} M_\odot$ which is at the higher halo mass regime than the HOD for central galaxies in Figure 8. Therefore, if the halo mass is larger than this $M_{\rm eff}$, we are able to conclude that satellite galaxies dominantly influence the clustering. Of LM samples, galaxies with $-10 <$ log sSFR/yr$^{-1} < -9$ show halo masses of $\sim 10^{13} h^{-1} M_\odot$. This means that these low sSFR LM galaxies mainly consist of satellites. In contrast, the halo mass for $-8.85 <$ log sSFR/yr$^{-1} < -8.5$ galaxies corresponding to the upper part of the main sequence is below $M_{\rm eff}$, which implies that the significant fraction of them is central galaxies.

However, in the case of HM galaxies, it is more complex than LM galaxies. From Figure 8, it can be seen that the central HOD spans a wide halo mass range. Moreover, the $M_{\rm eff}$ value for all HM galaxies is $10^{12.83} h^{-1} M_\odot$, and this is just above the peak of the central HOD. Therefore, we can reasonably expect a significant contribution from central galaxies to the clustering. From Figure 15, the overall trend for HM star-forming galaxies is similar to that for LM star-forming ones. However, all halo masses do not exceed the range of the central HOD of the middle panel in Figure 8, and correspond to halo masses of $N_{\rm c}(M_{\rm halo}) > N_{\rm s}(M_{\rm halo})$, except the highest sSFR bin. This also confirms that the important contribution of central galaxies to the clustering. What we also find is that the lowest halo mass appears in $-9.25 <$ log sSFR/yr$^{-1} < -8.85$, which is the lower sSFR bin than that for LM galaxies, and corresponds to the upper envelope of the star-forming main sequence in Figure 5.

Another striking feature is the halo mass of passive galaxies. We already discussed the dependence on stellar masses in the previous section. However, the halo mass of passive galaxies is also similar to $M_{\rm eff}$ of all galaxies in each stellar mass bin. This implies that the influence of central passive galaxies is also significant as well as satellites, even in the LM bin. Moreover, the halo masses for both stellar mass bins are within the range of central HODs in Figure 8. In fact, the fractions of passive galaxies are 24% and 50% in the LM and HM bins, respectively. Even if we assume that all satellites are passive galaxies, these values are much larger than the satellite fraction for all galaxies from the HOD in Figure 9, and confirm the substantial contribution of central passive galaxies to the clustering. Additionally, Krause et al. (2013) found that red central galaxies tend to be in slightly more massive halos than blue central galaxies based on SDSS data. Therefore, the higher halo mass for passive galaxies than main sequence ones can be explained by the high mass of halos hosting passive central galaxies as well as passive satellites.

The complexity of Figure 15 highlights the potential of HOD analysis to identify subtle environmental and evolutionary trends if a sufficiently large and well constrained sample of galaxies is studied. Based on our results for $M_* > 10^{10} M_\odot$ galaxies at $z \sim 1$, the clustering of main sequence galaxies, which shows the lowest halo mass, is most significantly affected by central galaxies. Given the hierarchical growth of structure and the expected evolution of main sequence star-

forming galaxies, it would be expected that these central galaxies could become satellite galaxies via accretion on to massive halos or remain as central galaxies with the assembly of stellar and halo masses. During this accretion, and while orbiting as satellites, they would undergo environmental quenching of their star formation (e.g., from ram pressure stripping, tidal harassment or starvation), which would explain the high halo masses associated with low sSFR galaxies. On the other hand, the population with enhanced star formation activity are in relatively massive halos of group like environments, and a subdominant population at $z \sim 1$. In our data, the fraction of $-8.5 < \log\ \mathrm{sSFR/yr^{-1}} < -8.0$ galaxies with $M_* > 10^{10} M_\odot$ is ~10% of all galaxies, which is similar to the measured merger rates at $z = 1$ from previous studies (Lotz et al. 2008; Bundy et al. 2009; Conselice et al. 2009; de Ravel et al. 2009; López-Sanjuan et al. 2009). Therefore, galaxy mergers play a subdominant role for the evolution of star-forming galaxies at this epoch, even if we assume all high sSFR galaxies experience mergers or interaction. Recently Moustakas et al. (2013) also concluded that galaxy mergers are not a dominant source of stellar mass growth at $z < 1$. Additionally, the significant fraction of passive galaxies are central ones which weakens the clustering strength compared to a satellite dominated sample. These passive central galaxies may originate in star-forming central galaxies passively evolving, or galaxy mergers with the central galaxy accelerating the consumption of gas.

Mostek et al. (2013) concluded that the secular processes are the dominant mechanism for the evolution of galaxies, which means that galaxies evolve from a low M_*–high sSFR to a high M_*–low sSFR regime through star formation within the galaxy, and that galaxy mergers play a subdominant role. Moreover, Tinker et al. (2013) claimed that the stellar mass function of passive central galaxies has significantly increased since $z = 1$, especially at $M_* < 10^{11} M_\odot$. Our results show that main sequence galaxies are mainly central galaxies, and a significant fraction of them evolve into low sSFR central galaxies together with the decreased star formation activity and the increased stellar and halo masses. Therefore, our result also supports the suggestion that the bulk of $M_* > 10^{10} M_\odot$ star-forming galaxies at $z \sim 1$ follow secular evolution (orange arrow in Figure 15) supplemented by minor mergers with galaxies fainter than our stellar mass limit accounting for the bulk of their growth. This was also suggested by Noeske et al. (2007) and Peng et al. (2010). Additionally, a similar trend was found at $z \sim 2$ (Lin et al. 2012; Sato et al. 2014) and the local universe (Li et al. 2008; Heinis et al. 2009) which implies that this is the main evolutionary mechanism of star-forming galaxies over the last 10 Gyr. Importantly, the magnitude limit of our survey allows us to detect both galaxies that would give rise to a major merger within any halo so in principle it would be possible to constrain the major merger rate once the redshifts of a representative sub-sample of pairs is determined.

7. SUMMARY AND CONCLUSION

In this work, we have used deep and wide data sets based on UKIDSS DXS and CFHTLS–Wide surveys to investigate the dependence of galaxy clustering on intrinsic properties and how galaxies are linked with their host halos. The main results are summarized as follows.

1. Using deep and wide near-IR/optical imaging data of the SA22 field, we have constructed a mass-limited sample of galaxies at $0.8 < z < 1.2$. The redshift selection is based on photometric redshifts, and galaxy properties such as stellar masses and sSFRs were derived using SED fitting. In total, this sample consists of 66,864 galaxies with $M_* > 10^{10} M_\odot$ and $\log\ \mathrm{sSFR/yr^{-1}} < -8$ in this redshift range.
2. Splitting the selected galaxies at different stellar mass thresholds, we measured the angular two-point correlation function and performed the halo modeling to link galaxies with host dark matter halos. We found that more massive galaxies reside in more massive halos, and tend to be central galaxies.
3. The HODs for stellar mass binned galaxies were calculated by those for stellar mass threshold samples. In all bins, satellites are predominantly in $>10^{13} h^{-1} M_\odot$ halos. Moreover, the mass of halos hosting central galaxies is higher for massive galaxies with a broader distribution in halo mass than that found for less massive galaxies.
4. The HODs for stellar mass binned samples were used to calculate the stellar mass to halo mass ratio for central and satellite galaxies separately. For central galaxies this ratio shows a peak at $\sim 10^{12} h^{-1} M_\odot$ that drops sharply above and below this halo mass, indicating the most efficient stellar mass growth at this peak halo mass. On the other hand, satellite galaxies significantly contribute to the total stellar mass in group and cluster environments.
5. We find an anti-correlation between bias and sSFR for low sSFR star-forming galaxies that are at or below the main sequence ($-10 < \log\ \mathrm{sSFR/yr^{-1}} < -8.5$), implying that star-forming galaxies at around the main sequence tend to live in a less massive halo ($M_{\mathrm{halo}} \sim 10^{12.5} h^{-1} M_\odot$) while low sSFR or passive galaxies are more likely to be in massive halos ($M_{\mathrm{halo}} > 10^{12.5} h^{-1} M_\odot$). However, we also see a reversal of this relation for galaxies in the highest sSFR bin ($-8.5 < \log\ \mathrm{sSFR/yr^{-1}} < -8$) that galaxies with the highest sSFRs are in dense environments. This can be seen regardless of the stellar mass of galaxies.
6. We speculate that the bulk of galaxies evolves from on or above the main sequence of star-forming galaxies to a lower sSFR regime as their mass assembles through forming new stars and minor mergers. Additionally, major mergers happen in relatively massive halos, and contribute to the galaxy evolution sub-dominantly at $z \sim 1$.

Our results are derived from deep and wide multiwavelength data sets. Nevertheless, this work is based on the only photometric data for relatively massive galaxies in a specific redshift bin and thus it is difficult to avoid contamination. In the future, deeper and wider data sets such as those from the UKIDSS, VISTA, Subaru Hyper-Suprime Camera, Pan-STARRS and LSST surveys will provide an opportunity to investigate more details about the relationship between various galaxy properties and their host dark matter halos with less massive galaxies and in various redshift bins. Additionally, spectroscopic surveys will also allow further progress on the clustering analysis. In terms of parameterized HODs, we have assumed that the central HOD becomes unity after a certain

halo mass. However, AGN feedback may change the shape of central HODs, especially the maximum mean number for central galaxies. Therefore it may also be necessary to modify the standard HOD work in order to directly compare observations and models once the samples have increased sufficiently.

The authors thank the referee for valuable comments improving the presentation and content of the paper. This work was supported by the National Research Foundation of Korea (NRF) grant, No. 2008-0060544, funded by the Korea government (MSIP). A.C.E. acknowledges support from STFC grant ST/I001573/1. We are grateful to UKIDSS team, the staff in UKIRT, Cambridge Astronomical Survey Unit and Wide Field Astronomy Unit in Edinburgh. The United Kingdom Infrared Telescope is run by the Joint Astronomy Centre on behalf of the Science and Technology Facilities Council of the UK Based on observations obtained with MegaPrime/MegaCam, a joint project of CFHT and CEA/DAPNIA, at the Canada–France–Hawaii Telescope (CFHT) which is operated by the National Research Council (NRC) of Canada, the Institut National des Science de l'Univers of the Centre National de la Recherche Scientifique (CNRS) of France, and the University of Hawaii. This work is based in part on data products produced at the Canadian Astronomy Data Centre as part of the Canada–France–Hawaii Telescope Legacy Survey, a collaborative project of NRC and CNRS.

Facilities: UKIRT, CFHT.

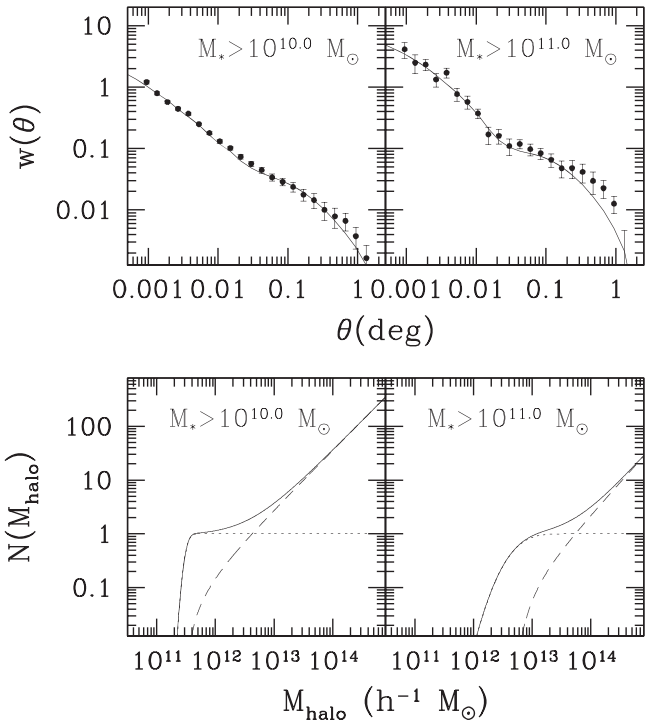

Figure 17. Same plot as Figure 6 for $M_* > 10^{10}M_\odot$ and $M_* > 10^{11}M_\odot$ galaxies. All symbols are the same as Figure 6. However, we used four free parameters for the halo modeling. As a result, the trend of derived parameters depending on M_* is same to Figure 6, although values are different.

APPENDIX A
HOD MODELING WITHOUT THE N_G CONSTRAINT

As desribed in Section 3.3, the halo model with three free parameters was applied to derive the property of halos hosting our galaxy sample. In this case, $M_{\rm cut}$ was determined by matching the observed galaxy number density with given parameters. In order to check the influence of this constraint to the best fit result, we investigate the best fit parameters without this constraint. Therefore, we perform the halo modeling for $M_* > 10^{10}M_\odot$ and $M_* > 10^{11}M_\odot$ galaxies with four free parameters ($\sigma_{\rm cut}$, $M_{\rm cut}$, M_0 and α). In this case, n_g is derived by the best fit HOD parameters describing the clustering only.

Figure 17 shows the angular correlation function (upper) and the HOD (lower) for each galaxy sample. All symbols are the same as Figure 6. However, the solid line in the upper panel and the HOD in the lower panel are the result based on the halo model with four free parameters. The best fit parameters are listed in Table 4. Comparing the values in Tables 1 and 4, the derived values of b_g and $M_{\rm eff}$ are identical, and other halo mass parameters also show the same trend. In addition, the central HOD for massive galaxies ($\sigma_{\rm cut} = 0.4$) still shows the gentler shape than that for low mass galaxies ($\sigma_{\rm cut} = 0.1$), which indicates that the constraint by the galaxy number density does not affect the trend of the fitting results.

However, $M_{\rm cut}$ and M_0 without the n_g constraint are approximately a factor of 2 smaller than those with the constraint, and $\sigma_{\rm cut}$ values also decrease from 0.5 and 0.6 to 0.1 and 0.4 for $M_* > 10^{10}M_\odot$ and $M_* > 10^{11}M_\odot$, respectively. In addition, the number densities calculated by the model without the constraint are higher than observed ones. This mismatch was already reported in Matsuoka et al. (2011) and Wake et al. (2011). Unfortunately, it is not yet answered what is the main reason leading to this mismatch. More studies are necessary to resolve this problem.

APPENDIX B
HALO MODELING VERSUS FITTING DARK MATTER CLUSTERING

In order to link galaxies to their host dark matter halos, we performed the halo modeling for stellar mass threshold samples and the direct fit of correlation functions of dark matters for stellar mass binned samples and sSFR binned samples. Here, we apply the later method to the stellar mass threshold samples, and then compare bias and halo mass from this fit (quoted as DM fit, hereafter) to the best fit result from the halo model. This comparison will provide a guideline for our analysis.

Figure 18 shows the comparison between the halo model (open symbols) in Table 1 and the fit of dark matter clustering (filled symbols). First, we are able to notice that the bias is consistent independently of the method (upper panel). However, in the case of halo masses, they show different results. The halo mass from the DM fit is close to $M_{\rm eff}$ from the halo model, but shows a discrepancy, especially for low mass galaxies. This is easily explained by the fraction of satellites, since satellites are in massive halos. In addition, $M_{\rm eff}$ is close to M_0 at the low stellar mass regime, but $M_{\rm cut}$ at the high mass regime, which is also explained by the same reason.

Although the bias estimated by fitting the dark matter clustering do not perfectly represent the mass of halos hosting galaxies selected, representative halo masses for central and satellite galaxies well bracket the halo mass by the DM fit. Therefore, the halo mass for central galaxies is always lower than that by the DM fit.

Table 4
The HOD Parameters for Stellar Mass Threshold Galaxies

Threshold (1)	σ_{cut} (2)	M_{cut} (3)	M_0 (4)	α (5)	n_g (6)	b_g (7)	M_{eff} (8)	f_{cen} (9)	χ^2/dof (10)
$10^{10.0}$	$0.10^{+0.0002}_{-0.0003}$	$11.501^{+0.001}_{-0.008}$	$12.593^{+0.012}_{-0.010}$	$1.10^{+0.02}_{-0.01}$	$135.1^{+5.8}_{-2.6}$	$1.59^{+0.03}_{-0.04}$	$12.757^{+0.036}_{-0.049}$	$0.77^{+0.02}_{-0.01}$	2.45
$10^{11.0}$	$0.40^{+0.0277}_{-0.0278}$	$12.692^{+0.017}_{-0.021}$	$13.697^{+0.029}_{-0.027}$	$1.20^{+0.13}_{-0.10}$	$7.1^{+1.6}_{-1.1}$	$2.26^{+0.14}_{-0.14}$	$13.115^{+0.101}_{-0.088}$	$0.92^{+0.03}_{-0.03}$	1.25

Note. However, the halo modeling is performed with four free parameters without the constraint by the Galaxy number density. All units are the same to Table 1.

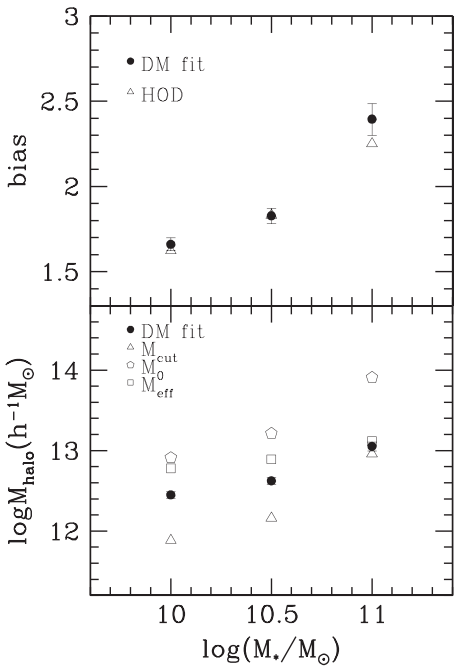

Figure 18. Comparison of results from the halo model (open symbols) and the fit of dark matter correlation function (filled symbols) for stellar mass threshold samples. Upper and lower panels are for bias and halo mass, respectively. For the display purpose, the errors from the halo model are not displayed (see Table 1 for these values).

REFERENCES

Arnouts, S., Cristiani, S., Moscardini, L., et al. 1999, MNRAS, 310, 540
Barton, E. J., Geller, M. J., & Kenyon, S. J. 2000, ApJ, 530, 660
Baugh, C. M. 2006, RPPh, 69, 3101
Behroozi, P. S., Conroy, C., & Wechsler, R. H. 2010, ApJ, 717, 379
Benson, A. J., Cole, S., Frenk, C. S., Baugh, C. M., & Lacey, C. G. 2000, MNRAS, 311, 793
Berlind, A. A., & Weinberg, D. H. 2002, ApJ, 575, 587
Bertin, E., & Arnouts, S. 1996, A&AS, 117, 393
Bertin, E., Mellier, Y., Radovich, M., et al. 2002, in ASP Conf. Ser. 281, Astronomical Data Analysis Software and Systems XI, ed. D. A. Bohlender, D. Durand, & T. H. Handley (San Francisco, CA: ASP), 228
Bezanson, R., van Dokkum, P., & Franx, M. 2012, ApJ, 760, 62
Bielby, R. M., Gonzalez-Perez, V., McCracken, H. J., et al. 2014, A&A, 568, 24
Blake, C., Collister, A., & Lahav, O. 2008, MNRAS, 385, 1257
Brammer, G. B., Whitaker, K. E., van Dokkum, P. G., et al. 2009, ApJ, 706, 173
Brown, M. J. I., Jannuzi, B. T., Dey, A., & Tiede, G. P. 2005, ApJ, 621, 41
Brown, M. J. I., Zheng, Z., White, M., et al. 2008, ApJ, 682, 937
Bruzual, G., & Charlot, S. 2003, MNRAS, 344, 1000
Bullock, J. S., Kolatt, T. S., Sigad, Y., et al. 2001, MNRAS, 321, 559
Bundy, K., Fukugita, M., Ellis, R. S., et al. 2009, ApJ, 697, 1369
Calzetti, D., Armus, L., Bohlin, R. C., et al. 2000, ApJ, 533, 682
Cappelluti, N., Allevato, V., & Finoguenov, A. 2012, arXiv:1201.3920
Casali, M., Adamson, A., Alves de Oliveira, C., et al. 2007, A&A, 467, 777
Chabrier, G. 2003, PASP, 115, 763
Chuter, R. W., Almaini, O., Hartley, W. G., et al. 2011, MNRAS, 413, 1678
Coil, A. L., Newman, J. A., Croton, D., et al. 2008, ApJ, 672, 153
Cole, S., Lacey, C. G., Baugh, C. M., & Frenk, C. S. 2000, MNRAS, 319, 168
Coleman, G. D., Wu, C.-C., & Weedman, D. W. 1980, ApJS, 43, 393
Conselice, C. J., Bundy, K., Trujillo, I., et al. 2007, MNRAS, 381, 962
Conselice, C. J., Yang, C., & Bluck, A. F. L. 2009, MNRAS, 394, 1956
Contreras, S., Baugh, C., Norberg, P., & Padilla, N. 2013, MNRAS, 432, 2717
Cooper, M. C., Coil, A. L., Gerke, B. F., et al. 2010, MNRAS, 409, 337
Cooper, M. C., Newman, J. A., Weiner, B. J., et al. 2008, MNRAS, 383, 1058
Cooray, A., & Sheth, R. 2002, PhR, 372, 1
Coupon, J., Kilbinger, M., McCracken, H. J., et al. 2012, A&A, 542, 5
Daddi, E., Cimatti, A., Pozzetti, L., et al. 2000, A&A, 361, 535
Daddi, E., Cimatti, A., Renzini, A., et al. 2004, ApJ, 617, 746
Daddi, E., Elbaz, D., Walter, F., et al. 2010, ApJ, 714, 118
de Ravel, L., le Févre, O., Tresse, L., et al. 2009, A&A, 498, 379
Drory, N., Bundy, K., Leauthaud, A., et al. 2009, ApJ, 707, 1595
Dye, S., Warren, S. J., Hambly, N. C., et al. 2006, MNRAS, 372, 1227
Elbaz, D., Daddi, E., le Borgne, D., et al. 2007, A&A, 468, 33
Ellison, S. L., Patton, D. R., Simard, L., & McConnachie, A. W. 2008, AJ, 135, 1877
Elston, R., Rieke, G. H., & Rieke, M. J. 1988, ApJ, 331, 77
Foucaud, S., Almaini, O., Smail, I., et al. 2007, MNRAS, 376, L20
Foucaud, S., Conselice, C. J., Hartley, W. G., et al. 2010, MNRAS, 406, 147
Franx, M., Labbé, I., Rudnick, G., et al. 2003, ApJ, 587, 79
Furusawa, J., Sekiguchi, K., Takata, T., et al. 2011, ApJ, 727, 111
Garilli, B., Le Févre, O., Guzzo, L., et al. 2008, A&A, 486, 683
Genzel, R., Tacconi, L. J., Gracia-Carpio, J., et al. 2010, MNRAS, 407, 2091
Gonzalez-Perez, V., Baugh, C. M., Lacey, C. G., & Almeida, C. 2009, MNRAS, 398, 497
Gonzalez-Perez, V., Baugh, C. M., Lacey, C. G., & Kim, J.-W. 2011, MNRAS, 417, 517
Grazian, A., Fontana, A., Moscardini, L., et al. 2006, A&A, 453, 507
Groth, E. J., & Peebles, P. J. E. 1977, ApJ, 217, 385
Guo, Q., & White, S. D. M. 2009, MNRAS, 396, 39
Gwyn, S. D. J. 2012, AJ, 143, 38
Hanami, H., Ishigaki, T., Fujishiro, N., et al. 2012, PASJ, 64, 70
Hartley, W. G., Almaini, O., Cirasuolo, M., et al. 2010, MNRAS, 407, 1212
Hartley, W. G., Almaini, O., Mortlock, A., et al. 2013, MNRAS, 431, 3045
Hartley, W. G., Lane, K. P., Almaini, O., et al. 2008, MNRAS, 391, 1301
Heinis, S., Budavári, T., Szalay, A. S., et al. 2009, ApJ, 698, 1838
Hickox, R. C., Jones, C., Forman, W. R., et al. 2009, ApJ, 696, 891
Hickox, R. C., Myers, A. D., Brodwin, M., et al. 2011, ApJ, 731, 117
Hwang, H. S., Elbaz, D., Dickinson, M., et al. 2011, A&A, 535, 60
Ideue, Y., Taniguchi, Y., Nagao, T., et al. 2012, ApJ, 747, 42
Ilbert, O., Arnouts, S., McCracken, H. J., et al. 2006, A&A, 457, 841
Ilbert, O., Capak, P., Salvato, M., et al. 2009, ApJ, 690, 1236
Ilbert, O., McCracken, H. J., le Févre, O., et al. 2013, A&A, 556, 55
Ilbert, O., Salvato, M., le Floc'h, E., et al. 2010, ApJ, 709, 644
Im, M., Lee, H. M., Lee, M. G., et al. 2008, in ASP Conf. Ser. 399, Panoramic Views of Galaxy Formation and Evolution, ed. T. Kodama, T. Yamada, & K. Aoki (San Francisco, CA: ASP), 382
Im, M., Yamada, T., Tanaka, I., & Kajisawa, M. 2002, ApJL, 578, L19
Jarvis, M. J., Bonfield, D. G., Bruce, V. A., et al. 2013, MNRAS, 428, 1281
Jing, Y. P., Mo, H. J., & Boerner, G. 1998, ApJ, 494, 1
Kampczyk, P., Lilly, S. J., de Ravel, L., et al. 2013, ApJ, 762, 43
Kim, H.-S., Baugh, C. M., Cole, S., Frenk, C. S., & Benson, A. J. 2009, MNRAS, 400, 1527
Kim, J.-W., Edge, A. C., Wake, D. A., et al. 2014, MNRAS, 438, 825
Kim, J.-W., Edge, A. C., Wake, D. A., & Stott, J. P. 2011, MNRAS, 410, 241
Kinney, A. L., Calzetti, D., Bohlin, R. C., et al. 1996, ApJ, 467, 38
Ko, J., Im, M., Lee, H. M., et al. 2012, ApJ, 745, 181
Kong, X., Daddi, E., Arimoto, N., et al. 2006, ApJ, 638, 72
Kong, X., Fang, G., Arimoto, N., & Wang, M. 2009, ApJ, 702, 1458
Krause, E., Hirata, C. M., Martin, C., Neill, J. D., & Wyder, T. K. 2013, MNRAS, 428, 2548

Kravtsov, A. V., Berlind, A. A., Wechsler, R. H., et al. 2004, ApJ, 609, 35
Lambas, D. G., Tissera, T. B., Sol Alonso, M., & Coldwell, G. 2003, MNRAS, 346, 1189
Landy, S. D., & Szalay, A. S. 1993, ApJ, 412, 64
Lawrence, A., Warren, S. J., Almaini, O., et al. 2007, MNRAS, 379, 1599
Lee, M. G., Lee, H. M., Im, M., et al. 2009a, in ASP Conf. Ser. 418, AKARI, a Light to Illuminate the Misty Universe, ed. T. Onaka, G. J. White, T. Nakagawa, & I. Yamamura (San Francisco, CA: ASP), 241
Lee, S.-K., Ferguson, H. C., Somerville, R. S., et al. 2014, ApJ, 783, 81
Lee, S.-K., Ferguson, H. C., Somerville, R. S., Wiklind, T., & Giavalisco, M. 2010, ApJ, 725, 1644
Lee, S.-K., Idzi, R., Ferguson, H. C., et al. 2009b, ApJS, 184, 100
Le Févre, O., Vettolani, G., Garilli, B., et al. 2005, A&A, 439, 845
Lewis, A., Challinor, A., & Lasenby, A. 2000, ApJ, 538, 473
Li, C., Kauffmann, G., Heckman, T. M., Jing, Y. P., & White, S. D. M. 2008, MNRAS, 385, 1903
Limber, D. N. 1954, ApJ, 119, 655
Lin, L., Dickinson, M., Jian, H.-Y., et al. 2012, ApJ, 756, 71
Loh, Y.-S., Rich, R. M., Heinis, S., et al. 2010, MNRAS, 407, 55
López-Sanjuan, C., Balcells, M., Pérez-González, P. G., et al. 2009, A&A, 501, 505
Lotz, J. M., Davis, M., Faber, S. M., et al. 2008, ApJ, 672, 177
Ma, C.-P., & Fry, J. N. 2000, ApJ, 543, 503
Magliocchetti, M., Lapi, A., Negrello, M., de Zotti, G., & Danese, L. 2014, MNRAS, 437, 2263
Matsuoka, Y., Masaki, S., Kawara, K., & Sugiyama, N. 2011, MNRAS, 410, 548
McCracken, H. J., Ilbert, O., Mellier, Y., et al. 2008, A&A, 479, 321
McCracken, H. J., Capak, P., Salvato, M., et al. 2010, ApJ, 708, 202
McIntosh, D. H., Guo, Y., Hertzberg, J., et al. 2008, MNRAS, 388, 1537
Meneux, B., Guzzo, L., de la Torre, S., et al. 2009, A&A, 505, 463
Meneux, B., Guzzo, L., Garilli, B., et al. 2008, A&A, 478, 299
Merson, A. I., Baugh, C. M., Helly, J. C., et al. 2013, MNRAS, 429, 556
Mihos, J. C., Richstone, D. O., & Bothun, G. D. 1992, ApJ, 400, 153
Mostek, N., Coil, A. L., Cooper, M., et al. 2013, ApJ, 767, 89
Moster, B. P., Somerville, R. S., Maulbetsch, C., et al. 2010, ApJ, 710, 903
Moustakas, J., Coil, A. L., Aird, J., et al. 2013, ApJ, 767, 50
Muzzin, A., Marchesini, D., Stefanon, M., et al. 2013, ApJ, 777, 18
Navarro, J. F., Frenk, C. S., & White, S. D. M. 1997, ApJ, 490, 493
Newman, J. A., Cooper, M. C., Davis, M., et al. 2013, ApJS, 208, 5
Nikoloudakis, N., Shanks, T., & Sawangwit, U. 2013, MNRAS, 429, 2032
Noeske, K. G., Weiner, B. J., Faber, S. M., et al. 2007, ApJ, 660, 43
Norberg, P., Baugh, C. M., Hawkins, E., et al. 2001, MNRAS, 328, 64
Norberg, P., Baugh, C. M., Hawkins, E., et al. 2002, MNRAS, 332, 827
Oi, N., Matsuhara, H., Murata, K., et al. 2014, A&A, 566, 60
Palamara, D. P., Brown, M. J. I., Jannuzi, B. T., et al. 2013, ApJ, 764, 31
Patton, D. R., Torrey, P., Ellison, S. L., Mendel, J. T., & Scudder, J. M. 2013, MNRAS, 433, 59
Peacock, J. A., & Smith, R. E. 2000, MNRAS, 318, 1144
Peebles, P. J. E. 1980, The Large-Scale Structure of the Universe (Princeton, NJ: Princeton Univ. Press)
Peng, Y.-J., Lilly, S. J., Kovač, K., et al. 2010, ApJ, 721, 193
Perez, J., Tissera, P., Padilla, N., Alonso, M. S., & Lambas, D. G. 2009, MNRAS, 399, 1157
Pipino, A., Cibinel, A., Tacchella, S., et al. 2014, ApJ, 797, 127
Popesso, P., Biviano, A., Finoguenov, A., et al. 2015, A&A, 574, 105
Quadri, R. F., Williams, R. J., Franx, M., & Hildebrandt, H. 2012, ApJ, 744, 88
Quadri, R. F., Williams, R. J., Lee, K., et al. 2008, ApJL, 685, L1
Roche, N. D., Almaini, O., Dunlop, J., Ivison, R. J., & Willott, C. J. 2002, MNRAS, 337, 1282
Roche, N. D., Dunlop, J., & Almaini, O. 2003, MNRAS, 346, 803
Roche, N., Eales, S. A., Hippelein, H., & Willott, C. J. 1999, MNRAS, 306, 538
Ross, A. J., & Brunner, R. J. 2009a, MNRAS, 399, 878
Ross, A. J., Percival, W. J., & Brunner, R. J. 2010, MNRAS, 407, 420
Ross, N. P., Shen, Y., Strauss, M. A., et al. 2009b, ApJ, 697, 1634
Sato, T., Sawicki, M., & Arcila-Osejo, L. 2014, arXiv:1407.2319
Sawangwit, U., Shanks, T., Abdalla, F. B., et al. 2011, MNRAS, 416, 3033
Schlegel, D. J., Finkbeiner, D. P., & David, M. 1998, ApJ, 500, 525
Scoccimarro, R., Sheth, R. K., Hui, L., & Jain, B. 2001, ApJ, 546, 20
Scoville, N., Arnouts, S., Aussel, H., et al. 2013, ApJS, 206, 3
Seljak, U. 2000, MNRAS, 318, 203
Smith, R. E., Peacock, J. A., Jenkins, A., et al. 2003, MNRAS, 341, 1311
Stern, D., Assef, R. J., Benford, D. J., et al. 2012, ApJ, 753, 30
Stern, D., Eisenhardt, P., Gorjian, V., et al. 2005, ApJ, 631, 163
Tinker, J. L., Leauthaud, A., Bundy, K., et al. 2013, ApJ, 778, 93
Tinker, J. L., Robertson, B. E., Kravtsov, A. V., et al. 2010, ApJ, 724, 878
Tomcjak, A. R., Quadri, R. F., Tran, K. J., et al. 2014, ApJ, 783, 85
van Dokkum, P. G., Labbé, I., Marchesini, D., et al. 2009, PASP, 121, 2
van Dokkum, P. G., Whitaker, K. E., Brammer, G., et al. 2010, ApJ, 709, 1018
Wake, D. A., Nichol, R. C., Eisenstein, D. J., et al. 2006, MNRAS, 372, 537
Wake, D. A., Sheth, R. K., Nichol, R. C., et al. 2008, MNRAS, 387, 1045
Wake, D. A., Whitaker, K. E., Labbé, I., et al. 2011, ApJ, 728, 46
Wang, L., & Jing, Y. P. 2010, MNRAS, 402, 1796
Whitaker, K. E., Labbé, I., van Dokkum, P. G., et al. 2011, ApJ, 735, 86
Whitaker, K. E., van Dokkum, P. G., Brammer, G., & Franx, M. 2012, ApJL, 754, L29
White, S. D. M., & Rees, M. J. 1978, MNRAS, 183, 341
Williams, R. J., Quadri, R. F., Franx, M., van Dokkum, P., & Labbé, I. 2009, ApJ, 691, 1879
Wuyts, S., Förster, S., Natascha, M., et al. 2011, ApJ, 742, 96
Yan, L., Choi, P. I., Fadda, D., et al. 2004, ApJS, 154, 75
Zehavi, I., Blanton, M. R., Frieman, J. A., et al. 2002, ApJ, 571, 172
Zehavi, I., Weinberg, D. H., Zheng, Z., et al. 2004, ApJ, 608, 16
Zehavi, I., Zheng, Z., Weinberg, D. H., et al. 2005, ApJ, 630, 1
Zehavi, I., Zheng, Z., Weinberg, D. H., et al. 2011, ApJ, 736, 59
Zentner, A. R., Hearin, A. P., & van den Bosch, F. C. 2013, arXiv:1311.1818
Zheng, Z., Berlind, A. A., Weinberg, D. H., et al. 2005, ApJ, 633, 791
Zheng, Z., Coil, A. L., & Zehavi, I. 2007, ApJ, 667, 760